ORIGINAL RESEARCH ARTICLE

Lateral variations in the signature of earthquake-generated deposits in Lake Iznik, NW Turkey

R. Gastineau[1,2,3] | P. Sabatier[3] | S. C. Fabbri[1] | F. S. Anselmetti[1] | P. Roeser[4] |
N. Findling[2] | M. Şahin[5] | S. Gündüz[5] | F. Arnaud[3] | S. O. Franz[4] | N. D. Ünsal[5] |
J. de Sigoyer[2]

[1]Institute of Geological Sciences and Oeschger Centre for Climate Change Research, University of Bern, Bern, Switzerland

[2]Univ. Grenoble Alpes, Univ. Savoie Mont Blanc, CNRS, IRD, IFSTTAR, ISTerre, Grenoble, France

[3]EDYTEM, Université Savoie Mont-Blanc, Université Grenoble Alpes, CNRS, Le Bourget du Lac, France

[4]Environmental Geology Group, Institute of Geosciences, Bonn University, Bonn, Germany

[5]Bursa Uludağ Üniversitesi, Fen-Edebiyat Fakültesi, Bursa, Turkey

Correspondence
R. Gastineau, Institute of Geological Sciences and Oeschger Centre for Climate Change Research, University of Bern, Baltzerstrasse 1+3, 3012 Bern, Switzerland.
Email: renaldo.gastineau@geo.unibe.ch

Abstract

Using lake-sediment cores to document past seismicity requires a comprehensive understanding of possible lateral variations in depositional processes. This study aims to reveal the lateral variations in earthquake-induced event deposits throughout Lake Iznik, a large lake located on the middle strand of the North Anatolian Fault. Based on stratigraphic, sedimentological and geochemical analyses of 14 sediment cores from two subbasins across the lake, five different types of event deposits (T1–T5) were identified and characterised. One event deposit type (T5) is restricted to a delta mouth, characterised by the occurrence of authigenic Fe-Mn carbonates and interpreted to result from flood events. The four other types of event deposits are characterised by their synchronicity between cores and their age consistency with historical earthquakes and are interpreted to be likely generated by earthquakes. The locally prominent 1065 CE historical earthquake that ruptured the sub-lacustrine Iznik Fault produced at least three different types of event deposits. One deposit type (T2) is only observed for this very local earthquake, implying that the type of event deposit might also depend on ground-motion parameters. At the lake scale, the occurrence of various event deposits depends on the flow distance from the source of sediment destabilisations to the coring site.

KEYWORDS
earthquakes, geochemistry, lacustrine palaeoseismology, lake sediment, sedimentary analyses, turbidites, Turkey, Türkiye

1 | INTRODUCTION

Lake sediments are valuable and continuous archives of past extreme climates and geodynamic events (Sabatier et al., 2022). They generally preserve deposits induced by high-energy currents (Beck, 2009; Chapron et al., 1999; Hage et al., 2017; Wilhelm et al., 2013). Lake sediment-based palaeoseismology, along with faults and other structures, allows a better understanding of past earthquakes beyond historical data that are restricted to several centuries. To use this method, it is first necessary to assess the origin of each type of event deposit recorded in the lake system (Avşar et al., 2015; Hage et al., 2017; Sabatier et al., 2022).

Turbidity currents in lakes can result from large subaquatic slope failures (Kremer et al., 2015; Strasser et al., 2013) or thin surficial remobilisation (Moernaut et al., 2017; Molenaar et al., 2021). Slope failures can generate mass-transport deposits such as slides, slumps, debris-flow deposits and/or distal turbidites (Haughton et al., 2009; Mulder & Alexander, 2001). Different trigger mechanisms, such as sediment loading, earthquake shaking or flooding, can produce turbidity flows with often very similar lithological expressions (e.g. fining-upwards grain size), making their differentiation from the sedimentary record alone difficult (Beck, 2009; Chapron et al., 1999; Polonia et al., 2017; Sabatier et al., 2017; Vandekerkhove et al., 2020).

To accurately understand the trigger mechanism of event deposits, it is critical to examine lake-wide sediment-flow dynamics by investigating several sediment cores from different locations in the lake (Sabatier et al., 2022). River input to the lake can trigger underflow/overflow/interflow or homopycnal flows depending on the density of the river water compared to that of the lake water and the lake stratification (Sturm & Matter, 1978). Among these types of flows, underflows, also called hyperpycnal flows, can generate turbidity currents that continuously flow from the river mouth along the slope to the basin floor (Mulder & Alexander, 2001; Wilhelm et al., 2015). Several studies have succeeded in discriminating flood-generated and earthquake-generated deposits based on their different characteristics, such as (1) grain-size parameters (Beck, 2009; Chapron et al., 1999; Praet et al., 2020; Sabatier et al., 2017; Wilhelm et al., 2013); (2) Mn accumulation in hyperpycnites due to enhanced bottom-water oxygenation leading to oxide accumulation (Sabatier et al., 2017; Wilhelm et al., 2016b) or (3) the spatial distribution of the event deposits in a given system. Flood-induced homopycnal flows are more evenly distributed from the river mouth over a large area (Wilhelm et al., 2015), while hyperpycnal flows are spatially restricted to the delta area (Jenny et al., 2014). In contrast, earthquake-generated turbidites tend to pond in the deepest parts of lakes, and they might be deposited synchronously in different basins

(Drab et al., 2012; McHugh et al., 2006) or different lakes in the same region (Chapron et al., 2016; Praet et al., 2017).

Earthquake-generated deposits in lakes are mainly controlled by the ground-motion parameters that depend on the distance from the seismic rupture, the magnitude, the amplitude of the low-frequency or high-frequency waves or the duration of shaking for example (McHugh et al., 2016; Moernaut et al., 2014, 2021). They also depend on *in situ* parameters such as the possible site effects (Van Daele et al., 2019; Vandekerkhove et al., 2020), sedimentation rate (Rapuc et al., 2018; Wilhelm et al., 2016a), geotechnical sediment properties (Yakupoğlu et al., 2022), slope angle and length (Zitter et al., 2012) and the potential effects of the tsunami or seiche that may be associated with the earthquake (Beck, 2009). To better use lake sediments to characterise earthquakes, it is essential to study the lateral lithological variations in event deposits (or lack of deposits) from these earthquakes, as several deposits can co-occur at different locations in the lake basin for the same earthquake. Lateral variations in earthquake-induced deposits between the slope and the basin have been studied in several lakes and marine systems to better understand the mechanism involved in turbidite formation (Lu et al., 2017; McHugh et al., 2016; Molenaar et al., 2021). They show that surficial remobilisation is an important process that creates turbidites in the case of a strong earthquake, even far from the rupture. Therefore, studying the type and spatial distribution of synchronous earthquake-generated event deposits is essential and can quantitatively provide information on the magnitude and location of prehistoric earthquakes using ground motion modelling, for example (Kremer et al., 2017; Vanneste et al., 2018).

This study investigates 14 sediment cores in two subbasins of Lake Iznik (Turkey), located on the middle strand of the North Anatolian Fault (MNAF), to characterise and understand the lateral variations in earthquake-generated deposits. Stratigraphic and multiproxy analyses were conducted on the 14 sediment cores to (1) correlate the sediment cores and event deposits; (2) distinguish the different types of event deposits according to their sedimentological and geochemical signatures; (3) highlight different depositional mechanisms, and finally, (4) investigate the spatial variation in chronologically well-constrained earthquake-generated event deposits related to an active underwater fault in the lake.

2 | CONTEXT

2.1 | Lake setting

Lake Iznik (83.5 m a.s.l, 40°26′N, 29°32′E) is located south-east of the Marmara Region (Bursa Province), east

of Gemlik Bay (Figure 1). It is the fifth largest lake in Turkey (Türkiye) and the largest lake in the Marmara Region, with N–S and E–W extents of 12 and 32 km, respectively. The lake has a catchment area of *ca* 1257 km^2 and a surface area of 313 km^2 (i.e. a small drainage basin-to-lake area ratio of four; Franz et al., 2006; Roeser, 2014). Two mountain ranges border the Iznik Basin: the Samanli Mountains (max. elevation 1227 m a.s.l.) to the north and the Katırlı Mountains (1275 m a.s.l.) to the south. They have different lithologies consisting of volcanic, metamorphic, mafic and carbonate rocks in the northern part and siliciclastic sediments with carbonate and felsic volcanic rocks in the south (Figure 1B; Viehberg et al., 2012).

Lake Iznik comprises three subbasins, according to the bathymetric map assembled by the General Directorate of Turkish Hydraulic Works (DSI; see Data Availability Statement). One subbasin is isolated in the western part of the lake (WSB; max depth 40 m), while an E–W elongated ridge separates the central-eastern part of the lake into two other subbasins in the north (NESB; max depth 45 m) and the south (SESB; max depth 75 m; Figure 1B). The main inflows are the Kocadere, Olukdere, Kurudere, Karadere and Kirandere (dere = river in Turkish; Figure 1B). The lake's outlet is the Göliataği dere, which flows westwards towards the Marmara Sea (Gemlik Bay). A thermocline occurs at approximately 15–20 m in the summer months, which deepens to 25–30 m until late December before the lake becomes fully mixed in the spring (Viehberg et al., 2012). In the northern and southern subbasins, during stratification, the dissolved oxygen concentration reaches hypoxic conditions (O_2 <1 mg/L) below *ca* 35–40 m due to the decomposition of organic material (Viehberg et al., 2012).

The sedimentation of Lake Iznik was first studied for palaeoclimate purposes (Franz et al., 2006; Miebach et al., 2016; Roeser et al., 2012, 2016; Ülgen et al., 2012). A *ca* 18 m long composite core section covering the last *ca* 31 kyr was collected from the ridge between the NESB and SESB (Roeser et al., 2016). In addition, many other shorter cores (*ca* 5 m in length) and surface sediments were recovered from other areas in the lake (Ülgen et al., 2012). The sediments of Lake Iznik were described as homogeneous silty clays consisting of three main components: siliciclastic (*ca* 83%), carbonate (*ca* 8%) and biogenic fractions (*ca* 9%) (Gastineau et al., 2021; Roeser, 2014 and references therein). The detrital fraction of lake sediments is composed mainly of quartz, feldspar (plagioclase), carbonates (aragonite and calcite) and clay minerals (smectite, illite, kaolinite and chlorite; Franz et al., 2006; Ülgen et al., 2012; Viehberg et al., 2012). Among the carbonate minerals, calcite is autochthonous and detrital, while aragonite is solely endogenic (Roeser et al., 2016; Viehberg et al., 2012). The biogenic fraction is defined by pollen and other plant remains and diatoms, cladocerans, chironomids and ostracods (Franz et al., 2006; Roeser, 2014).

2.2 | Tectonic settings and regional seismicity

Lake Iznik is bordered to the south by the MNAF (Figure 1). The North Anatolian Fault (NAF) is a 1500 km long right-lateral strike-slip fault that accommodates the westwards migration of the Anatolian microplate due to the Eurasian/Arabian collision (Çağatay & Uçarkuş, 2019; Reilinger et al., 2006; Şengör & Yilmaz, 1981). At its western termination, the NAF zone displays a complex organisation divided into three branches (Figure 1A). Its northern strand (NNAF) continues south of Istanbul through the Marmara Sea (Armijo et al., 2005). The MNAF is 148 km long, borders the south of two basins, the Geyve-Pamukova Basin and the Iznik Basin, and continues westwards along the Gemlik Gulf into the Marmara Sea (Figure 1B). The southern strand (SNAF) is less pronounced in the landscape and extends across the Bursa Province (Figure 1A). The NNAF has been seismically active in recent times: from 1939 to 1999, a sequence of fault ruptures (moment magnitude Mw >6.8) propagated westwards from Erzincan to Düzce and Izmit (Stein et al., 1997). Different studies on earthquake-generated turbidites in the different basins of the Marmara Sea suggest a recurrence time of 200–300 years for earthquakes of Ms ≥6.8 on the offshore segments of the NNAF (Çağatay et al., 2012; Drab et al., 2012, 2015; McHugh et al., 2006, 2014; Sarı & Çağatay, 2006; Yakupoğlu et al., 2019). Henry et al. (2021) monitored two earthquakes (24/09/2019 and 26/09/2019) in the Marmara Sea at a 5 km distance from their devices (a pressure recorder and a Doppler recording current meter) with Mw values of 4.7 and 5.8, respectively. They observed that only the later higher-magnitude event caused turbidite deposition, suggesting a magnitude threshold between 4.7 and 5.8 to generate turbidites in the Marmara Sea (for earthquakes with a rupture in the Marmara Sea). However, these turbidites did not reach the depocentre, which is an essential observation because this is where sediment cores are sampled for palaeoseismological purposes. On the MNAF, the instrumental seismicity shows no earthquakes during the last century. This observation contrasts with significant historical tectonic activity along the MNAF. Several chronicles and archaeological studies report the partial destruction of the city of Iznik (former Nicaea) and surrounding cities (Ambraseys, 2002; Ambraseys & Finkel, 1991; Ambraseys & Jackson, 2000). In addition, the geomorphological study of Benjelloun et al. (2021) along the MNAF shows that at least four earthquakes of magnitudes between 6.5 and
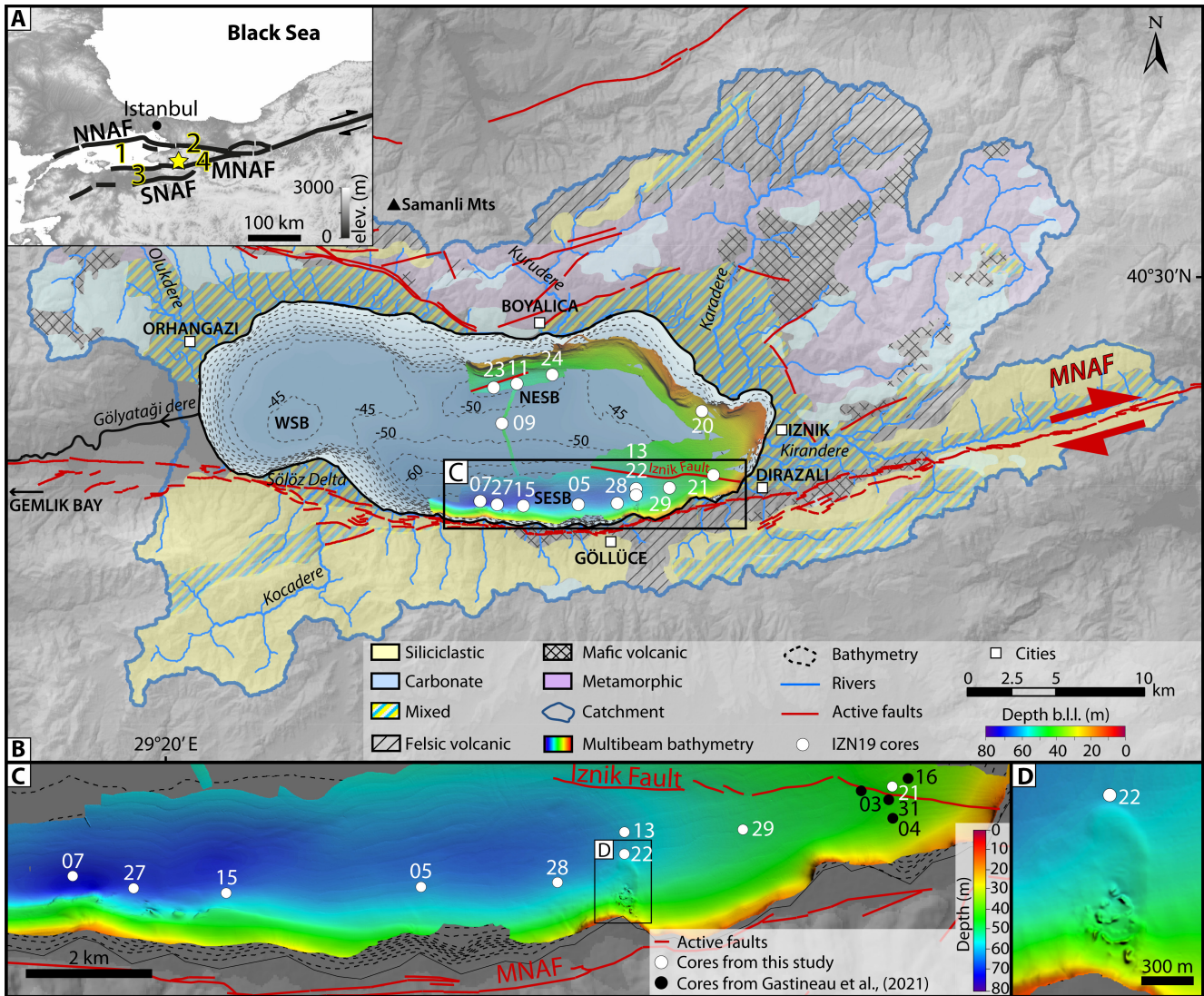
FIGURE 1 (A) SRTM DEM of the north-western part of Turkey. 1: Marmara Sea; 2: Lake Sapanca; 3: Bursa Province; 4: Geyve-Pamukova Basin. The yellow star denotes the location of Lake Iznik. NNAF, MNAF, and SNAF indicate the northern, middle and southern strands of the North Anatolian Fault. (B) Lithological map of the watershed of Lake Iznik (modified from Viehberg et al., 2012) and limits of its catchment (dark blue line). The hillshade relief is generated from the Shuttle Radar Topography Mission (SRTM—1 arc-second resolution; https://earthexplorer.usgs.gov/) digital elevation model (DEM). The main rivers are drawn in blue. The MNAF and other active faults are red (Benjelloun, 2017; Doğan et al., 2015; Gastineau et al., 2021; Öztürk et al., 2009). The dashed bathymetric contour lines in the lake represent 5 m intervals (Devlet Su İşleri [DSI]; General Directorate of Turkish Hydraulic Works), superimposed on the hillshaded bathymetry (2 m grid) from Gastineau et al. (2021), with a sun illumination angle/elevation of 20°N/45°. A vertical exaggeration of 15× was applied. The colour scale represents the depth below lake level (b.l.l.), based on a long-term reference lake level of 83.5 m a.s.l. White dots and label names document the locations of the cores sampled in the lake (Table S1). WSB, NESB and SESB refer to the western, north-eastern and south-eastern subbasin, respectively. (C) Magnified view of the bathymetric map in the SESB of Lake Iznik. White dots indicate the locations of the cores of this study, and black dots are core locations from Gastineau et al. (2021). (D) Magnified view of the delta collapse.

7.3 have occurred on the MNAF in the last 2000 years, which should be strong enough to remobilise sediment over the entire basin, compared to those measured by Henry et al. (2021). For the archaeoseismological study (Benjelloun et al., 2020), three damage episodes are evidenced in Iznik: (1) between the 6th and late 8th centuries CE, (2) between the 9th and late 11th centuries CE and (3) after the late 14th century CE. These damaging events can be related to earthquakes that occurred along the different strands of the NAF (Ambraseys, 2002).

Lake Iznik's bathymetric and high-resolution seismic reflection data reveal two subaquatic active faults: the

South Boyalıca Fault and the Iznik Fault, belonging to the MNAF system (Figure 1B; Gastineau et al., 2021).

Sediment cores sampled on both sides of the subaquatic Iznik Fault document an event deposit (present on each side of the fault) at the base of a stratigraphic unit with a vertical offset of *ca* 40 cm. This offset decreases upcore as it is gradually levelled out. Therefore, this feature is interpreted as the last rupture, corresponding to the 1065 CE historical earthquake (Gastineau et al., 2021). In addition, the same study revealed 14 earthquake-induced turbidites deposited during historical earthquakes from the past two millennia, including the 1065 CE earthquake (Gastineau et al., 2021). To characterise the past earthquake history, a detailed investigation of lateral variations in these event deposits is presented using new sediment cores throughout the lake.

3 | METHODOLOGY

3.1 | Bathymetry

One third of the lake's surface (*ca* 80.5 km^2) area was mapped on 18 survey days during April 2019 using a Kongsberg EM2040 multibeam echosounder (Kongsberg Maritime, Horten, Norway, provided by the University of Bern) in a single-head configuration (Gastineau et al., 2021) mounted on the hull of a fishing boat. Data were recorded using Kongsberg's SIS software, processed in HIPS/SIPS 10.4.13 software (University of Bern) and interpreted using ArcGIS 10.4.1. More details are given in Gastineau et al. (2021).

3.2 | Coring and lithological description

Fourteen short cores between 1.46 m and 3.57 m in length were collected from Lake Iznik in April and July 2019 using a UWITEC percussion gravity corer (Figure 1B and Table S1). Based on the preliminary bathymetric and seismic results, cores were recovered from strategically selected locations (Gastineau et al., 2021). The cores were split into working/sampling and archive halves in the laboratory. Each core was photographed after oxidation to improve the visibility of different facies. Afterwards, a detailed sedimentological description was performed. The lithological description allowed different sedimentary facies and structures to be identified and the cross-correlation of the cores. Colours were assigned based on Munsell's colour chart (Munsell Color, 1994).

3.3 | Sedimentary analyses and geochemistry

3.3.1 | Grain-size analyses

The grain-size distribution of the event deposit was analysed at a 5 mm resolution for seven cores (IZN19_13, 20, 21, 22, 24, 27, 29). A Beckman Coulter Life Science 13 230 XR laser particle-size analyser (EDYTEM Laboratory, University Savoie Mont-Blanc) was used with sonication to avoid particle flocculation. Two runs with a 30 s measurement were applied without any pre-treatment. Grain-size parameters were directly extracted from Adapt software V. 1.3.337 and Gradistat V9.1 (Blott & Pye, 2001). The sorting index was calculated according to Folk and Ward (1957).

3.3.2 | Geochemistry

Geochemical analyses provide essential information about material provenance and potential biochemical modification (Arnaud et al., 2012; Rapuc et al., 2022). The relative content of major and trace elements was analysed using a rhodium anode with an X-ray fluorescence (XRF) Avaatech Core Scanner (EDYTEM Laboratory). The split-core surface was first covered with a 4 μm thick Ultralene film to avoid contamination and desiccation of the sediment. The scanning was performed at different resolutions (1, 2 or 5 mm), depending on the relative heterogeneity of each core, as evaluated with the naked eye (Table S1). Different settings were used to measure different elements: the cores were scanned at 10 kV/0.2 mA for 15 s to detect Al, Si, S, K, Ca and Ti and at 30 kV/0.3 mA for 20 s to detect Mn, Fe, Ni, Cu, Zn, Br, Rb, Sr, Zr and Pb (Richter et al., 2006). Due to its higher water content, core IZN19_20 was measured at 10 kV/0.1 mA for 15 s and then 30 kV/0.115 mA for 20 s. Single element relative abundances are expressed as centred log-ratios (CLRs) to avoid compositional effects inherent to this data type (Weltje et al., 2015; Weltje & Tjallingii, 2008) and calculated using the following equation:

$$CLR(X) = \ln \frac{X \text{ counts}(z)}{g(z)}$$

where 'X counts (z)' represents the counts for element X measured at depth z, and '$g(z)$' represents the geometric mean of the composition at depth z, calculated as follows:

$$g(z) = \sqrt[n]{\text{counts}_{\text{elements 1}} \cdot \text{counts}_{\text{elements 2}} \cdot \ldots \cdot \text{counts}_{\text{elements } n}}$$

Twelve elements were used to calculate the geometric mean: Al, Si, K, Ca, Ti, Mn, Fe, Zn, Br, Rb, Sr and Zr. Four

elements, S, Ni, Cu and Pb, were not used because they did not show well-defined fluctuations. However, the ratios were ln-transformed to avoid matrix effects such as grain-size dependency (Weltje & Tjallingii, 2008; Weltje et al., 2015). The mean and maximum values of the elements presented in the manuscript have been calculated from the bottom to the top of each studied event deposit.

A principal component analysis (PCA) was performed on the non-transformed XRF data of the complete sediment cores (background sedimentation and event deposits) (Sabatier et al., 2010). In addition, R software version 3.5.1 (Lê et al., 2008; R Core Team, 2018) was used to find potential correlations between the different elements measured, and principal sediment end-members were visually identified and used to better constrain each sedimentological facies (Sabatier et al., 2010).

3.3.3 | Scanning electron microscopy and energy-dispersive spectroscopy

To complement the core description, representative 8–10 cm long slabs, including different event-deposit types, were resin-embedded to produce thin sections. The samples were analysed with a Vega3 Tescan scanning electron microscope (ISTerre Laboratory, University Grenoble Alpes) with 10 and 16 kV tension after being covered with a 20 nm thick graphite layer. Representative areas were also analysed with an EDS probe (Rayspec with SamX electronic system and software, ISTerre Laboratory) to assess the chemical composition and map chemical elements.

3.3.4 | Loss on ignition

The loss on ignition (LOI) analyses were performed on the IZN19_15, 24 and 31 sequences (Figure S1), with a 10 cm sampling interval all along the sequence to estimate organic matter (OM) and carbonate content in the sediment, following the protocol described by Heiri et al. (2001). The sediment samples were dried and crushed before being heated in an oven at 550°C for 4 h and at 950°C for 2 h. The relative weight loss during the first and second heating phases corresponds to the OM (LOI550) and carbonate content (LOI950), respectively.

3.4 | Chronology

3.4.1 | Radiocarbon dating

Radiocarbon analyses of 35 organic plant macro-remains (*ca* 2 per sediment core) were performed at the Poznan

Radiocarbon Laboratory spectrometry. The ^{14}C ages were calibrated using the Intcal20 calibration curve using 2-sigma ranges (Reimer et al., 2020). Calibrated ages are expressed on the common era (CE) timescale: CE for the common era and BCE before the common era (Table 1). Well-constrained age models and sedimentation rate curves are presented in Gastineau et al. (2021).

3.4.2 | Tephra geochemistry

The occurrence of geochemically identified tephras allowed the age-depth model to be refined by comparison with the previously established history of volcanic ash deposition in the lake and its surroundings (Çağatay et al., 2015; Roeser et al., 2012). Tephra layers were polished on thin sections, and the glass shards were geochemically characterised using a JEOL JXA-8230 Electron Probe X-ray Micro Analyser (EMPA; ISTerre Laboratory, University Grenoble Alpes) equipped with five wavelength-dispersive spectrometers (WDSs) and one EDS detector using 15 kV voltage, 2 nA beam current, and 5–7 μm beam size. For standardisation, MPI-DING glasses (StHs6/80-G, GOR132-G; Jochum et al., 2000, 2005), natural minerals and synthetic oxides were used. Two glasses, Atho-G (Jochum et al., 2000, 2005) and KE-12 (Metrich & Rutherford, 1992), were analysed with the samples to verify analytical accuracy and exclude the loss of alkalis. This study did not include analyses of glass shards yielding a total oxide sum of less than 96%, suggesting they might contain mineral impurities. Analytical data were normalised to 100% total oxide values to enable comparison.

4 | RESULTS

4.1 | Bathymetry

Most of the lake's morphological features, such as two prominent lineaments interpreted as faults, have already been described by Gastineau et al. (2021). Here, the focus is on the southern shore, where recent scarps and a delta collapse were identified (Figure 1C). The SESB is delimited by the main strand of the MNAF to the south (on land), the E–W Iznik Fault to the north, the shore to the east and the Sölöz Delta to the west (Figure 1B). All cores were taken in areas with slopes of less than 1°. However, their distance from significant slopes (>30°) differs (Figure 1B,C). South of cores IZN19_07, _15 and _27, an undated submerged terrace occurs at *ca* 40 m below the present lake level with slopes reaching 30°, showing a fresh scarp *ca* 400 m south of core IZN19_27 (Figure 1C). Eastward, near the city of Göllüce, a significant delta

TABLE 1 Radiocarbon ages of the Lake Iznik sediment cores.

Sample name	Core	MCD (cm)	Radiocarbon age (yr BP)	Age cal BCE/CE 2σ range
Poz-118212	IZN19_05	134.00	285 ± 30	1500–1794 CE
Poz-117973	IZN19_07	117.25	335 ± 30	1475–1640 CE
Poz-117974	IZN19_07	158.50	390 ± 30	1442–1631 CE
Poz-118214	IZN19_09	105.50	640 ± 30	1285–1397 CE
Poz-117987	IZN19_09	305.50	3115 ± 30	1447–1286 BCE
Poz-117986	IZN19_11	77.50	890 ± 30	1045–1223 CE
Poz-117337	IZN19_11	138.00	1630 ± 35	364–545 CE
Poz-117982	IZN19_13	53.50	100 ± 30	1683–1930 CE
Poz-117983	IZN19_13	150.00	970 ± 30	1022–1159 CE
Poz-117984	IZN19_13	218.00	1205 ± 30	704–941 CE
Poz-117985	IZN19_13	258.75	1460 ± 30	564–650 CE
Poz-120185	IZN19_15	72.00	1250 ± 30	674–877 CE
Poz-117976	IZN19_15	127.50	1605 ± 30	415–544 CE
Poz-117978	IZN19_15	143.75	1675 ± 30	256–530 CE
Poz-117979	IZN19_15	156.50	2045 ± 30	154 BCE–58 CE
Poz-120186	IZN19_15	237.50	2600 ± 35	829–591 BCE
Poz-117980	IZN19_15	281.00	3610 ± 30	2115–1887 BCE
Poz-129012	IZN19_20	69.00	1510 ± 70	421–651 CE
Poz-129014	IZN19_20	128.00	1600 ± 30	416–545 CE
Poz-118973	IZN19_21	70.50	1345 ± 30	643–775 CE
Poz-118627	IZN19_21	245.50	2385 ± 30	719–393 BCE
Poz-118625	IZN19_22	87.00	190 ± 60	1530 CE–out of range
Poz-123273	IZN19_22	164.50	1130 ± 30	774–994 CE
Poz-118622	IZN19_23	86.20	90 ± 30	1687–1926 CE
Poz-118624	IZN19_23	133.00	1270 ± 510	482 BCE–1648 CE
Poz-118620	IZN19_24	97.50	1620 ± 30	406–543 CE
Poz-118621	IZN19_24	189.50	1955 ± 35	41 BCE–203 CE
Poz-118746	IZN19_27	84.20	975 ± 30	998–1159 CE
Poz-118748	IZN19_27	120.50	1060 ± 30	895–1030 CE
Poz-118706	IZN19_27	166.00	1290 ± 35	657–821 CE
Poz-118707	IZN19_27	261.70	1545 ± 30	433–592 CE
Poz-118686	IZN19_27	318.50	1650 ± 30	262–537 CE
Poz-118745	IZN19_28	74.00	300 ± 30	1495–1656 CE
Poz-118743	IZN19_29	104.00	1320 ± 30	652–775 CE
Poz-118744	IZN19_29	173.50	1585 ± 30	419–550 CE

Note: All measurements were made on plant remains.

Abbreviations: BP, before present, i.e. before 1950 CE. MCD, master composite depth.

collapse is visible in the bathymetry, showing mass movement of blocks with heights of *ca* 6 m and lengths of 20–100 m (Figure 1D). A halo at a distance of approximately 1 km could also be observed. Its lobe is semi-circular with a clear front that vertically rises from the undisturbed basin sediments by *ca* 1 m. Unfortunately, core IZN19_22 was collected *ca* 50 m too far to the north to penetrate this deposit. Eastward, near the Iznik Fault, other deltas are observed. The bathymetric map shows small scarps but no trace of massive event deposits on the lake floor, indicating that they are older or of a smaller scale than the one previously described (Figure 1C). In the Iznik Fault area, cores IZN19_21 and _31 are *ca* 1 km away from the slopes and separated by a topographic step *ca* 1 m in height due to the Iznik Fault that lies in between both cores (Figure 1C; Gastineau et al., 2021). In the northern

subbasin, an underwater terrace occurs at *ca* 40 m below the current lake level, similar to the one in the south, and causes lateral morphological variations. While the cliff is steeper north of core IZN19_23, it is less pronounced to the north of core IZN19_24. However, a slight depression between the terrace and core IZN19_23 is caused by the South Boyalıca Fault (Gastineau et al., 2021).

4.2 | Lithostratigraphy and geochemistry

4.2.1 | Background sediments

Based on naked-eye observations, grain size and geochemical analyses, three lithological facies have been described for background sedimentation (Gastineau et al., 2021). Facies I consists of brown (5Y/4/4, Munsell colour) (Munsell Color, 1994) silty clay (D50 *ca* 10 μm) and occurs at the top of the cores. Facies II consists of light brown (2.5Y/5/4) coarser-grained silt (D50 *ca* 15 μm). Finally, Facies III has olive-grey (5Y/6/2) fine silt (D50 *ca* 8 μm). These facies are sporadically interrupted by different event-deposit types, as described in Section 4.2.2.

A PCA from the sediment cores′ elemental composition presents two end-members for most cores. The first end-member indicates in-lake/endogenic processes (Ca, Sr, Br), and the second end-member indicates terrestrial input (e.g. Ti, Si, Al, K). A third end-member (Mn) might indicate redox/early diagenetic processes but occurs only in two cores (IZN19_20 and _27) (Figure S2). The PCA highlights the characteristics of each facies (Figure S2). Facies I is intermediate with a relatively more significant endogenic end-member influence. Facies II is highly influenced by the endogenic process end-member, characterised by high Ca, Sr and Br counts. In contrast, Facies III presents high terrigenous content.

4.2.2 | Event deposits

This study divided the event deposits into five types based on naked-eye observations. The five event-deposit types (T1–T5) are presented in Figure 2 with the grain-size data, geochemical data (Ti, Ca, Mn, Zr) and SEM images, including chemical mapping. The SEM observations combined with EDS analyses allowed the different phases present in each event-deposit type to be described. Geochemical analyses provide provenance information that can occasionally be influenced by grain size. Therefore, grain-size analyses were used to discuss the flow energy during deposition of an event deposit and characterise its transport and depositional mechanisms. Based on the PCA of different cores in different subbasins, the $\ln(Ca/Ti)$

ratio indicates in-lake processes (high Ca counts) versus terrestrial input (high Ti counts) (Figure S2; Gastineau et al., 2021) and holds information about the sediment origin. However, considering only the event deposits, calcium appears to be related to the coarsest grains (typically when grains are coarser than *ca* 100 μm, they are likely calcite; Figure 2A,C). In contrast, Ti is associated with intermediate to fine grains, as classically observed in other systems (Bertrand et al., 2012). Figure 3C presents the $\ln(Ca/Ti)_{mean}$ ratio calculated at the depth corresponding to $D90_{max}$ for each event deposit, often referring to the maximum peak-flow energy (Bøe et al., 2006; Molinaroli et al., 2009; Parris et al., 2010). The $\ln(Ca/Ti)_{mean}$ versus $D90_{max}$ shows the same increasing trend for all samples, with increasing $D90_{max}$, confirming that this ratio in the event deposits could be interpreted as an indicator of grain size. On the other hand, the $\ln(Zr/K)$ ratio seems to depend on grain size as well, except for the coarsest grains ($D50 > 150$ μm; Figure 2A).

- A single T1 event deposit occurs in core IZN19_27 at 3.20 m depth. It consists of a 6 cm thick sandy deposit ($D50_{max} = 280$ μm) that presents a fining upwards trend (D50 varies from *ca* 280 μm to 100 μm) and a sharp erosive contact with the underlying background sediments. This layer also incorporates shell fragments (Figure 2A). The Sorting Index versus D90 data show that the T1 deposit is better sorted than the others (Figure 3B). Manganese is present in T1 in association with the coarser-grained components of the deposit. The Mn counts show slightly higher values throughout the deposit. On the other hand, the Ti counts show a sharp decrease at the base of the deposit, overlain by a gradual upwards increase (Figure 2A). The Ca values are high at the bottom of the event deposit and decrease upwards. The $\ln(Ca/Ti)$ ratio thus reflects the grain-size profile well. However, the $\ln(Zr/K)$ ratio shows constant and intermediate values at the bottom of the deposit, where the grains are coarser (medium sand), and higher but decreasing values for the upper part of the deposit, where finer sediments are observed (very fine sand) (Figure 2A). The T1 deposit is also unique, as shown in the SEM images, as carbonate shells and calcite grains result in a high Ca EDS response. (Figure 2A). A rare occurrence of Fe and Mn coatings was also observed around carbonate grains.

- The T2 event deposits are 3–7 cm thick (Figure 2B). The base of the deposits is made of a 1 cm thick sandy fining-upwards layer, overlain by a layer *ca* 5 cm thick made of heterogeneous silt with patches of very fine sand ($D50_{max}$ range from 20 μm to 80 μm), and includes abundant plant macro-remains restricted to the top and bottom of the deposit (Figure 2B). For
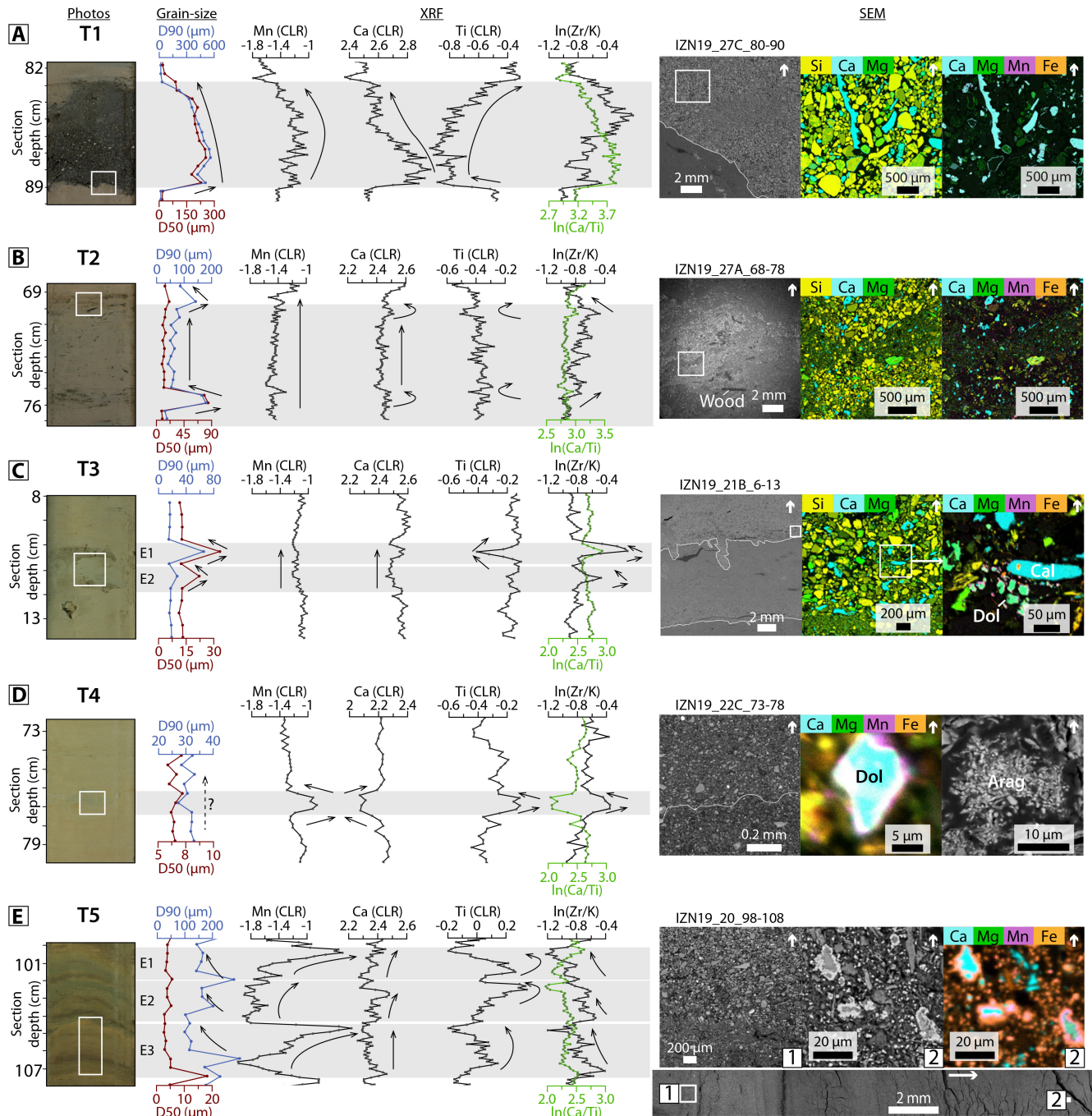
FIGURE 2 Characteristics of the different types of event deposits (T1–T5) found in the sedimentary sequences. From left to right: Optical photograph of a portion of the core, D50 and D90 trends (grain size), Mn, Ca, Ti counts, ln(Zr/K) and ln(Ca/Ti) (XRF data) and SEM/EDS images. Note that the scales do not have the same absolute values but show the same relative differences. Black arrows show the evolution of the parameters within a deposit. Blue rectangular areas highlight event deposits. The dots on the grain size and XRF data curves show the sampling intervals. White arrows in the SEM images show the top of the sedimentary sequence. White boxes in the photographs represent the location of the main SEM image, and the white boxes in the main SEM images show the location of the EDS mapping.

one third of the T2 deposits, another 1 cm thick sandy coarsening-upward layer is present on top. The classic D50 versus D90 diagram (Passega, 1964) shows that T2 deposits have a more significant increase in D90 than in D50, excluding two outliers that correspond to the base of the T2 deposits (Figure 3A). These three

layers are also reflected in the geochemical data. However, these data show only slight changes: the coarser-grained parts of the deposits are characterised by slightly lower Ti/higher Ca counts, whereas the central part of the deposit shows stable but higher Ti/lower Ca counts. Manganese shows constant values.
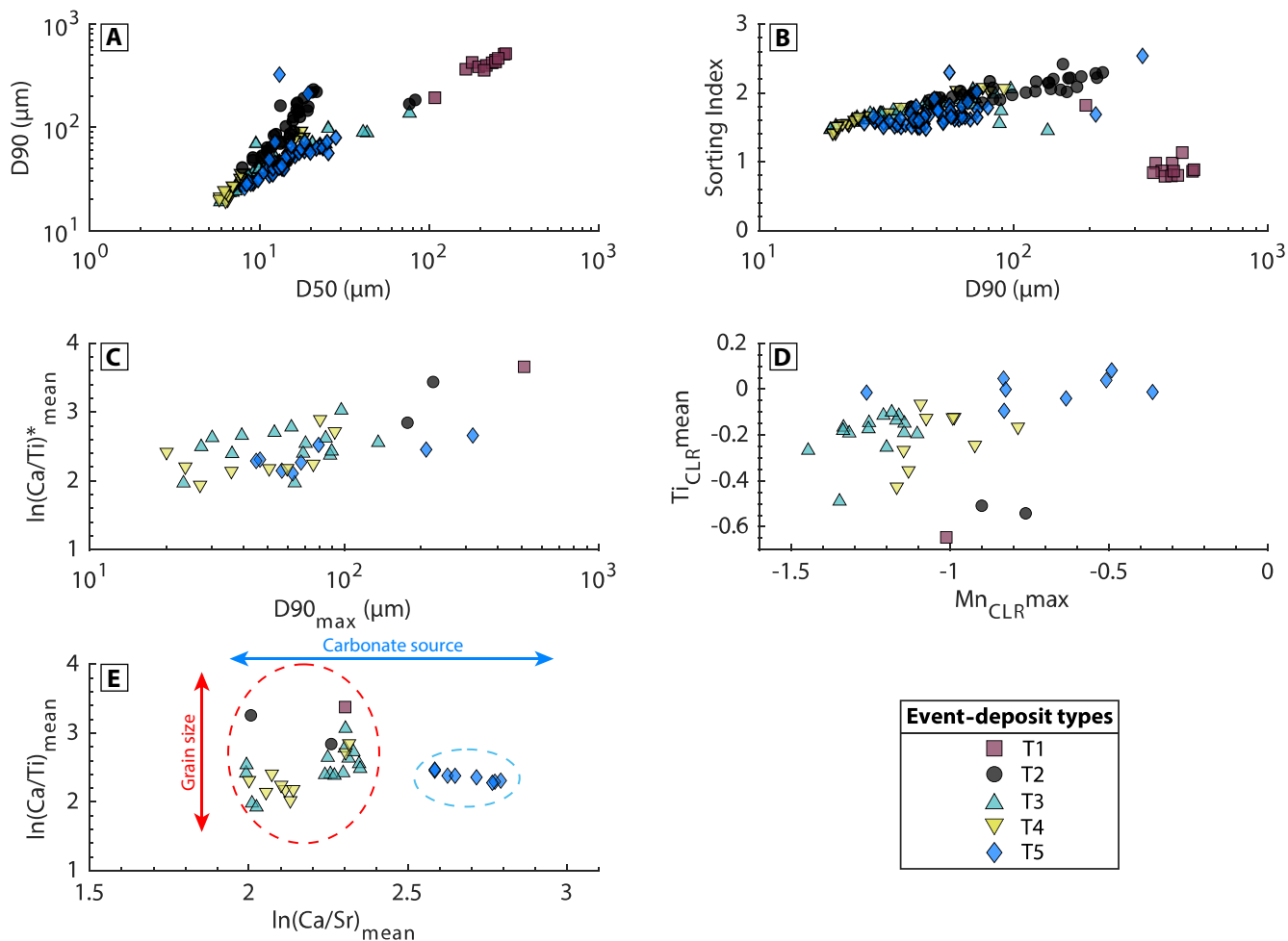
FIGURE 3 Diagrams with selected grain-size parameters and geochemical data for each event-deposit type. (A) D50 versus D90 diagram; (B) D90 versus sorting index diagram; (C) $D90_{max}$ versus $ln(Ca/Ti)*_{mean}$ diagram; (D) Mn_{max} versus Ti_{mean}; (E) $ln(Ca/Ti)_{mean}$ versus $ln(Ca/Sr)_{mean}$ diagram. Note that grain-size data are displayed on a logarithmic scale. Diagrams (C–E) display fewer data points because of the different resolutions of the grain-size data (5 mm) and the geochemical data (1–2 mm). '*' denotes that the ratio has been calculated at the depth corresponding to $D90_{max}$.

The ln(Zr/K) ratio is slightly higher than those within the background sedimentation. In contrast, the ln(Ca/Ti) ratio is constant (Figure 2B). The SEM/EDS observations also highlight the chaotic nature of this type of deposit. Sporadic Mn-Fe-rich spots were observed by SEM (Figure 2D). The T2 deposits are only reported in three sedimentary sequences, that is in cores IZN19_15, _24 and _27 (SESB and NESB).

- Most T3 event deposits appear macroscopically as millimetre-scale silty layers ($D50_{max}$ varies from 7 μm to 30 μm). Two are shown in Figure 2C. These event deposits also present fining-upward trends that are observable at the microscopic scale (Figure 2C). Detailed SEM observations show that some of these deposits have an erosive base, differentiating them from the T2 and T4 deposits. Bioturbation with vertical burrows occurs at the base of some deposits (Figure 2C). The burrows vary between 1 mm and 4 mm in length.

They are filled with particles from the overlying layers (Figure 2C). Here, two different end-member indicators (Mn and Ca) show slightly lower values than the background sedimentation. In contrast, Ti shows a drop for the coarser T3 deposit (E1 in Figure 2C) but constant values for the T3 deposit below (E2 in Figure 2C). While the ln(Zr/K) ratio seems to reflect the grain-size profile since a peak is observed at each event depth, the ln(Ca/Ti) ratio here only identifies the coarsest sandy layer (D50> *ca* 20 μm) where large calcite grains (*ca* 100 μm) occur (Figure 2C). Calcium further occurs as aragonite (characterised by small needles), calcite and dolomite phases (Figure 2C). Manganese is sporadically present around dolomites (e.g. Figure 2C). The T3 deposits are more common in the sedimentary sequences than the two previous deposits: *ca* 44 occurrences have been observed across most (9/14) cores at different depths.

- The T4 event deposits are made of silty lenses (a few millimetres thick) ($D50_{max}$ ranges from 6 μm to 20 μm) embedded within the background sediments. At the macroscopic scale, these deposits are characterised by blue/grey patches (GLEY1/6/1) of irregular shape (Figure 2D). At the microscopic scale, the boundary between the background sedimentation and the silty patches is challenging to identify (Figure 2D). Manganese, Ti and the ln(Zr/K) ratio show maximal values. In contrast, Ca and the ln(Ca/Ti) ratio are lower within the patches relative to the background sediments. Manganese and Fe have been observed in very small amounts in oxide coatings and as Mn-Fe carbonates around dolomite grains (e.g. Figure 2D). At the same time, Ca occurs in the aragonite, calcite and dolomite phases (Figure 2D). The T4 deposits are observed at *ca* 37 occurrences in eight out of 14 cores.

- The T5 event deposits occur 13 times and are only observed in core IZN19_20. Three are shown in Figure 2C. They show a fining upward trend from medium to fine silt and contain coloured laminated sequences. A brown coarser-grained part characterises the base of each T5 deposit ($D50_{max}$ ranges from 13 μm to 28 μm), illustrated by a higher ln(Zr/K) ratio. The Ca counts increase slightly upwards. The T5 deposits show a complex evolution at a microscopic scale: at their base, a centimetre-thick upwards fining deposit is overlain by finer sediments containing pulses of coarser-grained deposits. The ln(Ca/Ti) ratio shows no clear trend. However, the brown coarser-grained base is covered by a grey/blue Ti-rich lamina and a white Mn-rich layer that forms the top of each T5 event deposit (Figure 2E). All the carbonates and dolomites of this layer are rich in Mn and Fe (Figure 2E). The SEM analyses show that Mn and Fe are associated with the carbonate phases present in this layer type (Figure 2E). The maximum Mn relative abundance (CLR) highlights the occurrence of a Fe-Mn-carbonate solid solution or Mn coating on dolomites within these event deposits (Figure 3D). In comparison to the other event-deposit types, the T5 deposits reveal enrichment in Mn and Ti (Figure 3D) and have significantly higher values in the ln(Ca/Sr)$_{mean}$ plot (Figure 3E).

4.3 | Chronology

4.3.1 | Radiocarbon dating

Thirty-five organic terrestrial plant macro-remains were dated (Table 1). In the northern basin, the cores record a maximum of *ca* 2000 years at 2.25 m sediment depth (IZN19_24; Figure 4A), corresponding to a mean sedimentation rate of 1.13 mm/year. On the ridge in the lake's centre, the sedimentation rate is slightly lower (1 mm/year) as the core records *ca* 3500 years over 3.50 m (IZN19_09; Figure 4B), which agrees with previous studies (*ca* 3000 years in 3.50 m; Ülgen et al., 2012). Cores from the southern subbasin record a period ranging from *ca* 600 to 4000 years. Core IZN19_27, from the southern and deeper basin of the lake, has the highest sedimentation rate (1.88 mm/year), with *ca* 2000 years over 3.75 m (Figure 4D), while core IZN19_15, also located in the southern basin, records *ca* 4000 years over a 2.95 m long sequence, corresponding to a sedimentation rate of 0.74 mm/year (Figure 4D). An earlier study determined that Lake Iznik's sedimentation rate varies through time, following different phases during the last two millennia (Gastineau et al., 2021). First, a period with a relatively high and constant sedimentation rate from 0 to 350 cal. CE (*ca* 1.3 mm/year). Then, from 350 to 600 cal. CE, the sedimentation rate significantly increased, reaching 2.2 mm/year. After that, it decreased to *ca* 0.4 mm/year until the 11th century, when it stabilised (Gastineau et al., 2021). These values were calculated by correlating the radiocarbon ages of IZN19_03, 04, 16 and 31 on the IZN19_21 core to build a well-constrained model. The absolute values of sedimentation rates vary between locations in the lake, probably due to the size of the lake and its different river inputs. However, the relative trend remains the same.

4.3.2 | Tephrochronology

A tephra layer has been previously found in Lake Iznik and the Marmara Sea and is correlated to the Avellino tephra of Somma-Vesuvius/Italy (Çağatay et al., 2015; Roeser et al., 2012, 2016; Figure 5). This tephra is dated to 3945 ± 10 cal year BP, that is 1995 ± 10 cal year BCE (Sevink et al., 2011). A tephra layer with the same geochemical composition (Figure 5) is identified in the two cores that extend the furthest back in time: a 0.5 cm thick brown coarse ash layer occurs at 3.31 m in core IZN19_09, and a thin black layer defines its base. At 2.50 m in core IZN19_15, the same tephra layer is defined as a heterogeneous *ca* 0.5–1.5 cm thick and irregular coarse ash layer. The tephra contains abundant microcrystal-rich, high-vesicular micropumices that are phonolitic to tephriphonolitic.

4.4 | Core-to-core correlation

The core-to-core correlation allows an event-to-event correlation between different cores. These correlations can indicate the sensitivity of a given subbasin to ground shaking and changes in the flow regimes of turbidity currents. Based on lithological descriptions, XRF measurements and
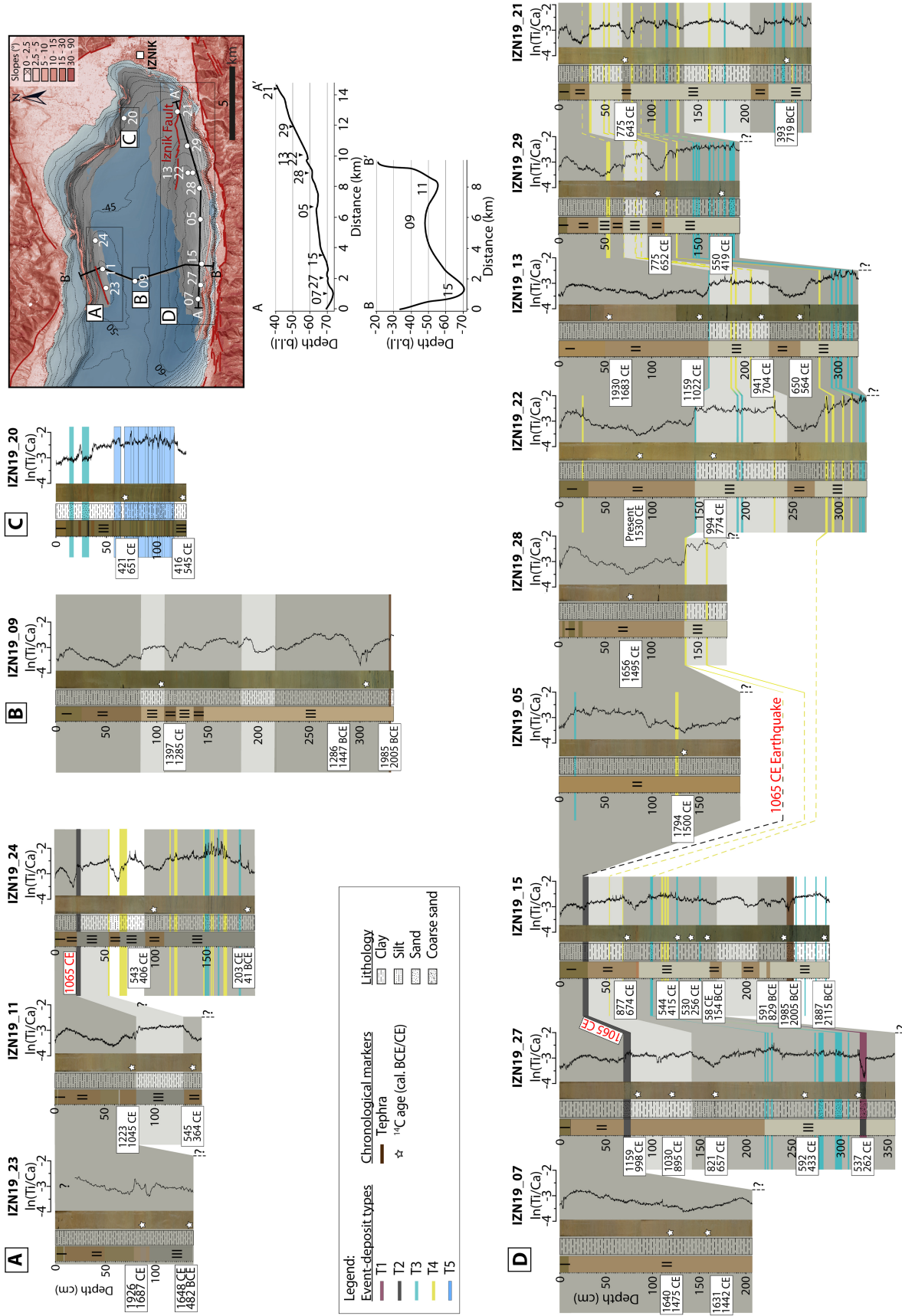
FIGURE 4 Lithological description and core-to-core correlation, photograph and ln(Ti/Ca) ratio of each core. The cores are grouped by lake subbasin: (A) the northern subbasin, (B) the ridge, (C) near the two submerged deltas and (D) the southern subbasin. Their locations are displayed on the map on the top right. I, II and III denote the different facies, and event deposits are displayed with horizontal coloured bars.
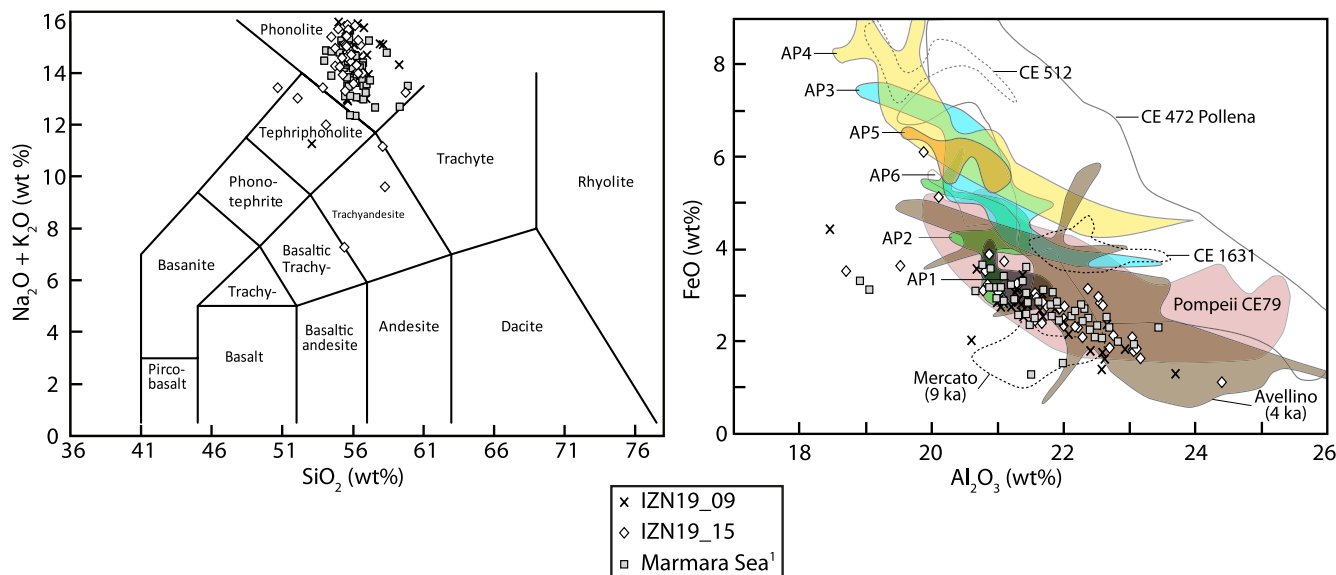
FIGURE 5 The geochemical composition of tephra samples from cores IZN19_09 and _15 (data from Lake Iznik, this study) and the Marmara Sea ([1]data from Çağatay et al., 2015). Left: SiO_2 versus Na_2O+K_2O diagram (Le Maitre et al., 1989). Right: Al_2O_3 versus FeO diagram (modified from Çağatay et al., 2015). Samples from both cores best matched Avellino tephra of Somma-Vesuvius/Italy, dated to 3945 ± 10 cal yr BP (Sevink et al., 2011) (details in Table S2).

radiocarbon dating, facies and event deposits are correlated across different subbasins (Figure 4). The correlation between the different facies of background sedimentation is possible because they show the same climate-controlled long-term fluctuations (Roeser et al., 2012; Ülgen et al., 2012) and similar sedimentary facies within the different subbasins. However, this is not the case for event deposits, whose occurrence and characteristics appear to be highly dependent on the core location, even at the intra-subbasin scale (Figure 4). Gastineau et al. (2021) show that different historical earthquakes are recorded in Lake Iznik (29-32, 69, 121, 269, 358, 362 or 368, 407, 447, 478, 554, 869, 989, 1065 CE); some of these occurred on the MNAF (29-32, 121, 368; 1065) while the others were linked to the NNAF. Correlating a deposit with a unique earthquake is sometimes difficult as the region presents high historical seismicity, and the radiocarbon-based age model does not allow an annual or even decadal resolution.

Figure 6 shows the spatial and temporal variations in the event records for different examples. For this purpose, vertical timescales for the sediment cores and swath profiles are presented. The only T1 observed in the sedimentary sequences of this study occurs in core IZN19_27 at *ca* 400 m from a >30° slope (Figure 6A,D). Similarly, this core records seven T3 deposits and a T2 deposit, the latter corresponding to the 1065 CE earthquake (Figures 4D and 6D). Core IZN19_15 also records a T2 deposit at *ca* 300 m from a >30° slope, generated by the same earthquake (Figure 6A,E), while core IZN19_24 records the same deposit but is more distant from steep slopes (*ca* 800 m; Figure 6C).

Lateral variations can be observed, for example, in cores IZN19_22 and IZN19_13, where T3 deposits evolve into T4 deposits towards the northern site (i.e. towards an area further away from steep slopes [>30°] Figure 6G). In contrast, in the northern subbasin of the lake, core IZN19_23 does not show any deposits in its *ca* 300 years-long record (Figure 6B).

4.5 | Calibration: Event deposits of the historic 6.8/VIII 1065 CE Iznik earthquake

Based on core studies, Gastineau et al. (2021) demonstrated that the destructive earthquake of September 1065 CE (Ambraseys, 2002) ruptured the Iznik Fault in Lake Iznik. This earthquake was, therefore, local and strong enough to have caused significant damage to the city of Iznik (Ambraseys, 2002). Based on historical and archaeological data, this earthquake had an estimated magnitude of 6.8 and a minimum intensity of VIII in the city (Ambraseys, 2002; Benjelloun et al., 2020). The stratigraphic, geochemical and age correlations between the sampled cores in Lake Iznik show that this local earthquake was recorded in most of the cores (7/10 sediment cores recording up to this period) but with different types of event deposits (i.e. T2, T3 and T4; Figure 4). Notably, this earthquake is the only one to have generated T2 deposits in cores IZN19_15, _24 and _27 (Figure 7). Of the three cores that do not record this earthquake (IZN19_09, 11, 29), one is located in the centre of the lake; therefore far from the coast, one in the NESB and one in the SESB (Figure 4). If we focus on the southern
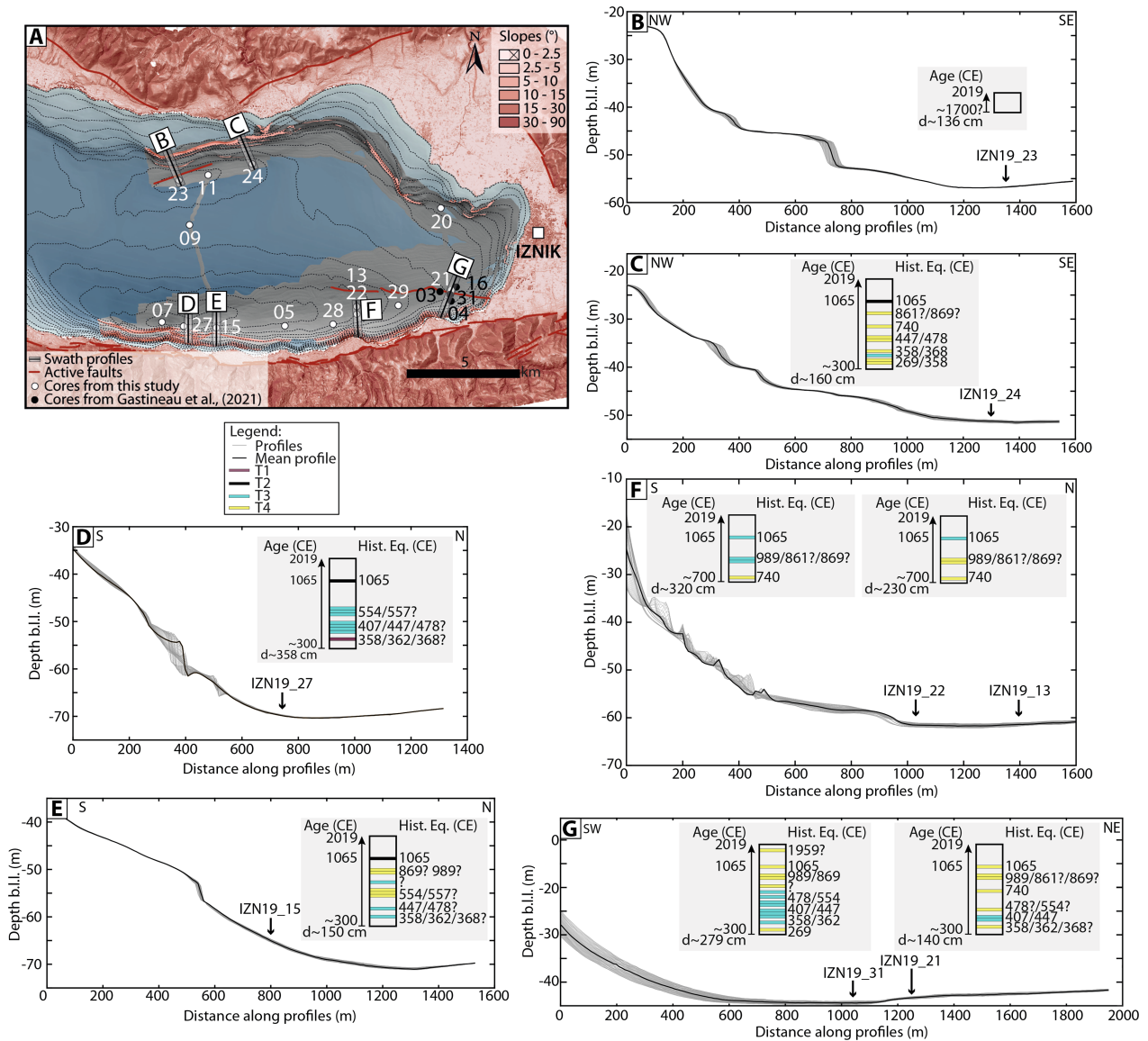
FIGURE 6 (A) The slope map of the basin's eastern part and the Lake Iznik watershed. White dots indicate the location of sediment cores presented in this study, while the black dots are from Gastineau et al. (2021). Active faults are drawn in red (Benjelloun, 2017; Gastineau et al., 2021). The terrestrial DEM and associated slope map are recovered from Pleiades photographs (Benjelloun et al., 2021). (B, C, D, E, F and G) Swathe profiles perpendicular to fault structures or cliffs to highlight the distance of selected sediment cores (IZN19_13, _15, _21, _22, _23, _24, _27 and _31). Swathe profiles are taken every 10 m in a 200 m wide profile. The black boxes aim to compare the event-deposit content from *ca* 300 years CE, when possible, and identify the possible matches with historical earthquakes. Please note that the vertical scale corresponds to ages. Variations in sedimentation rates are, therefore, best represented in Figure 4.

basin where it is most represented, the spatial distribution of 1065 CE deposits indicates lateral variations related to a unique and coseismic slope destabilisation. Three zones can be distinguished based on observations of the event-deposit types (Figure 7):

a. Cores IZN19_27 and _15 are located in the deepest basin within 1.5 km of each other (Figure 7A). Core IZN19_27 shows the thickest T2 deposit with 7 cm, which occurs just in front of a fresh slope scarp observed in the bathymetric map (Figure 7E). The

IZN19_15 sequence, located north of the scarp, contains a thinner T2 deposit of 5 cm.

b. Eastwards, another cluster of cores is grouped in a small area within a radius of 650 m (IZN19_28, _22 and _13; Figure 7B). Lateral variations in the event deposit types are also observed near the significant delta collapse in cores IZN19_22 and _13, collected at the foot of the landslide and 300 m further in the basin (Figure 7B), respectively. Both cores contain T3 deposits, while core IZN19_28 (1.2 km westwards) shows no deposits related to this earthquake.
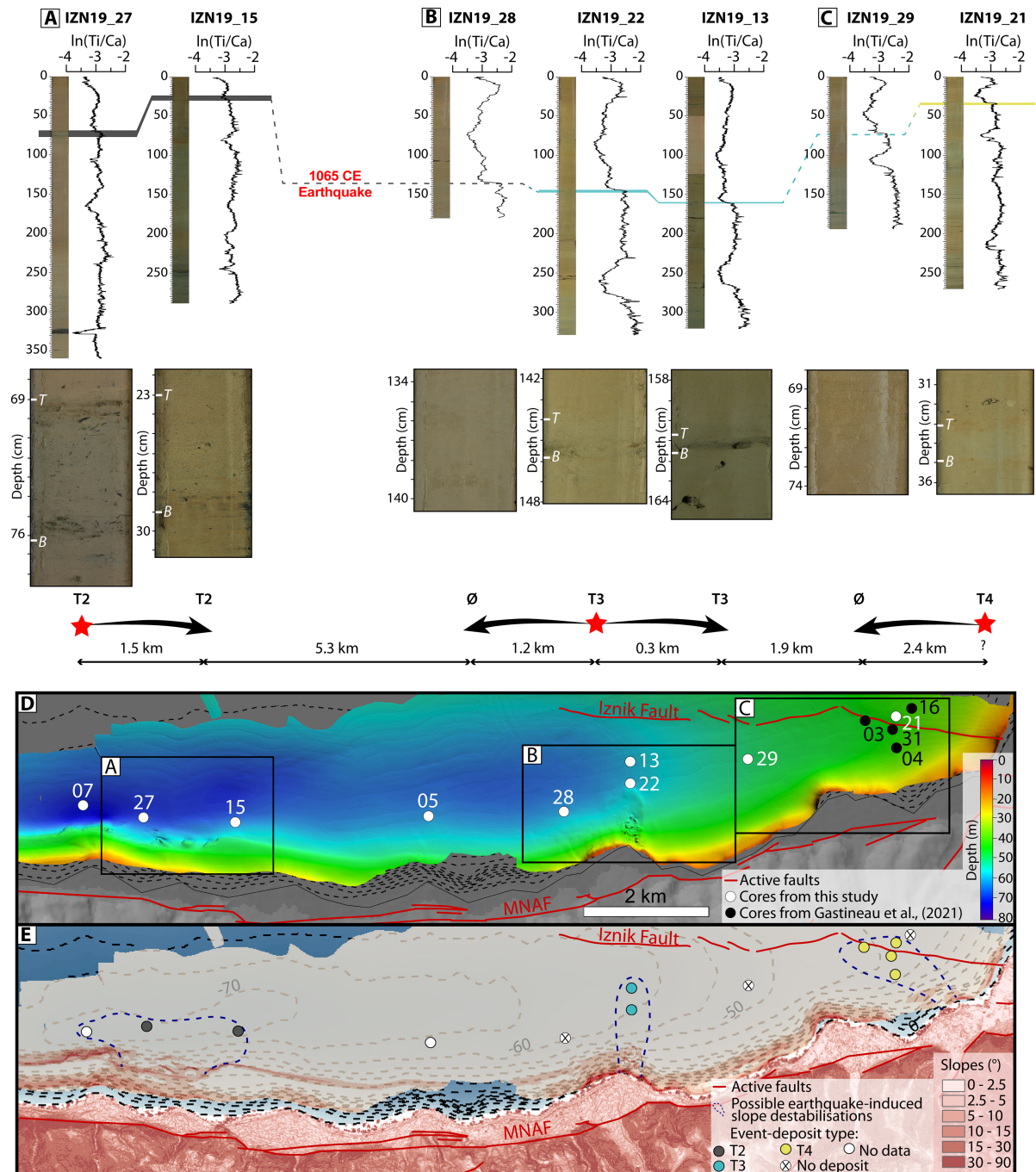
FIGURE 7 Data from an E–W transect of sediment cores, including photography and the Ti/Ca ratio. The coloured laminae correspond to different event-deposit types generated by the 1065 CE seismic event described by Gastineau et al. (2021). The colours are the same as those in Figure 4. A photograph of the core at the related event deposit depth is displayed. The bottom and top of the event deposits are denoted as 'B' and 'T' on the photographs, respectively. The type of event deposit and the distance between cores are displayed below each core. The red stars indicate the presumed nearest core from possible slope destabilisation(s) (details in the text). (A), (B) and (C) represent the different areas (see (D) for location) that synchronously recorded distinct event-deposit types from independent slope destabilisations (see text for details). (D) Bathymetric map of the southern part of Lake Iznik. White dots indicate the locations of study cores, and black dots show core locations from Gastineau et al. (2021) (E) Slope map retrieved from the bathymetric map. Coloured dots indicate the type of event deposits generated by the 1065 CE earthquake. Active faults are shown in red (Benjelloun, 2017; Gastineau et al., 2021). Blue dotted lines show the multiple possible sources of slope destabilisation with their extents related to the 1065 CE earthquake based on observations of the event-deposit types. Cores IZN19_07 and _05 are not displayed in this figure, as they are too short to record the 1065 CE earthquake (Figure 4). The onshore DEM and associated slope map were retrieved from Pleiades photographs (Benjelloun et al., 2021).

c. More than 2 km eastwards from zone (b), cores IZN19_29, _21, and four cores described in Gastineau et al. (2021) record another spatial distribution of event deposits. The easternmost core, IZN19_16 and core IZN19_29 (Figure 7C) do not show any event deposits that correlate with the 1065 CE historical earthquake, whereas all the other cores of this cluster (IZN19_03, _04, _21 and _31) show a T4 event deposit.

5 | DISCUSSION

5.1 | Sources of background sedimentation and event deposits

The geochemical analyses of the sediments show that at the scale of the sediment core, two main end-members can be defined in the last two millennia, in agreement with previous studies (Gastineau et al., 2021; Roeser et al., 2012; Ülgen et al., 2012), and these help to unravel the sediment sources (Figure S2). One end-member indicates in-lake/endogenic processes (Ca, Sr, Br), where Br is correlated with the organic fraction, i.e. LOI550 in Figure S1, which in the Holocene is often attributed to algal biomass (seen by lower C/N ratios; Roeser et al., 2016). Previous research indicated that Sr strongly correlates with aragonite and is closely linked to endogenic calcium carbonate in Lake Iznik's water (Roeser et al., 2016). In contrast, calcite is linked to both endogenic and detrital inputs (Roeser, 2014). A second end-member indicates terrestrial input (e.g. Ti, Si, Al, K) and a third end-member (Mn) might indicate redox/early diagenetic processes but occurs only in two cores (IZN19_20 and _27) (Figure S2).

However, $\ln(Ca/Ti)_{mean}$ as a function of $D90_{max}$ shows, for all samples, the same increasing trend with increasing $D90_{max}$. This trend indicates that this ratio strongly depends on the grain size of the coarsest fraction, i.e. with a diameter larger than ca 50 μm (Figure 3C). Thus, at the scale of the event deposit, the $\ln(Ca/Sr)$ ratio is used to differentiate between plagioclase and/or carbonate input from the catchment and in-lake carbonate production without any grain-size dependency (Figure S3 and Figure 3E). Figure 3E shows two end-members; the first one is characterised by low $\ln(Ca/Sr)$ ratios indicating predominantly aragonite (T1, T2, T3 and T4 event deposits) corresponding to higher contents of lacustrine carbonates (red dashed circle in Figure 3E) indicating that these event deposits comprise lacustrine sediments that have been reworked. However, the $\ln(Ca/Ti)$ ratio has a grain-size dependency, and this is reflected in Figure 3E, with T3 and T4 having finer grains and a lower $\ln(Ca/Ti)$ ratio, while T2 and T1 are characterised by coarser grains and a higher $\ln(Ca/Ti)$ ratio. The second end-member is characterised by higher $\ln(Ca/Sr)$ ratios (T5

event deposits), suggesting enrichment in detrital carbonates, i.e. calcite (blue dashed circle in Figure 3E), or perhaps plagioclase. The T5-type deposits also show enrichment in Mn and Ti (Figure 3D), which suggests that these event deposits probably have a different sediment source. Their higher Ti content is consistent with the less significant amount of Sr, suggesting that T5 deposits contain more detrital material than the other types of deposits.

5.2 | Depositional mechanisms of event deposits

5.2.1 | T1 depositional processes

The 6 cm thick T1 deposit occurs only once in a core located ca 1000 m from the shoreline but only ca 400 m from an underwater terrace's ca 30° slopes (IZN19_27; Figure 1C and Table S1). There is no matrix in the deposit (Figure 2); thus, it is interpreted to have been deposited by a flow dominated by grain-to-grain support.

The T1 deposit is erosional, shows pronounced normal grading and is better sorted than the other deposits (Figures 2A and 3). Therefore, it matches the deposits resulting from a concentrated density flow described by Mulder and Alexander (2001). In addition, experiments show that concentrated density flows produce thicker deposits than their dilute counterparts, matching the observations reported on here; T1 is the thicker deposit observed in the sediment cores (Mulder & Alexander, 2001; Figure 2). The difference between a hyperconcentrated flow and a concentrated density flow is that in the latter, particles settle freely in the flow, which eventually produces normal grading, as observed in the T1 deposit. Concentrated density flows are similar to high-density turbidity currents described by Talling et al. (2012).

Thus, it is possible to conclude that T1 deposits are produced by either a concentrated density flow (Mulder & Alexander, 2001) or by a high-density turbidity current (Talling et al., 2012) originating from the steep southern slopes (Figure 8A).

5.2.2 | T2 depositional processes

The T2 deposits show a different path on the D90/D50 diagram than the other types of deposits (Figure 3A), as they have a skewed distribution with coarse grains in a fine-grained matrix. Combined with a lack of grading, this grain-size pattern supports the interpretation that T2 layers were deposited by cohesive debris flows (Mulder & Alexander, 2001; Talling et al., 2012), with matrix support as a dominant particle-support mechanism and with a flow
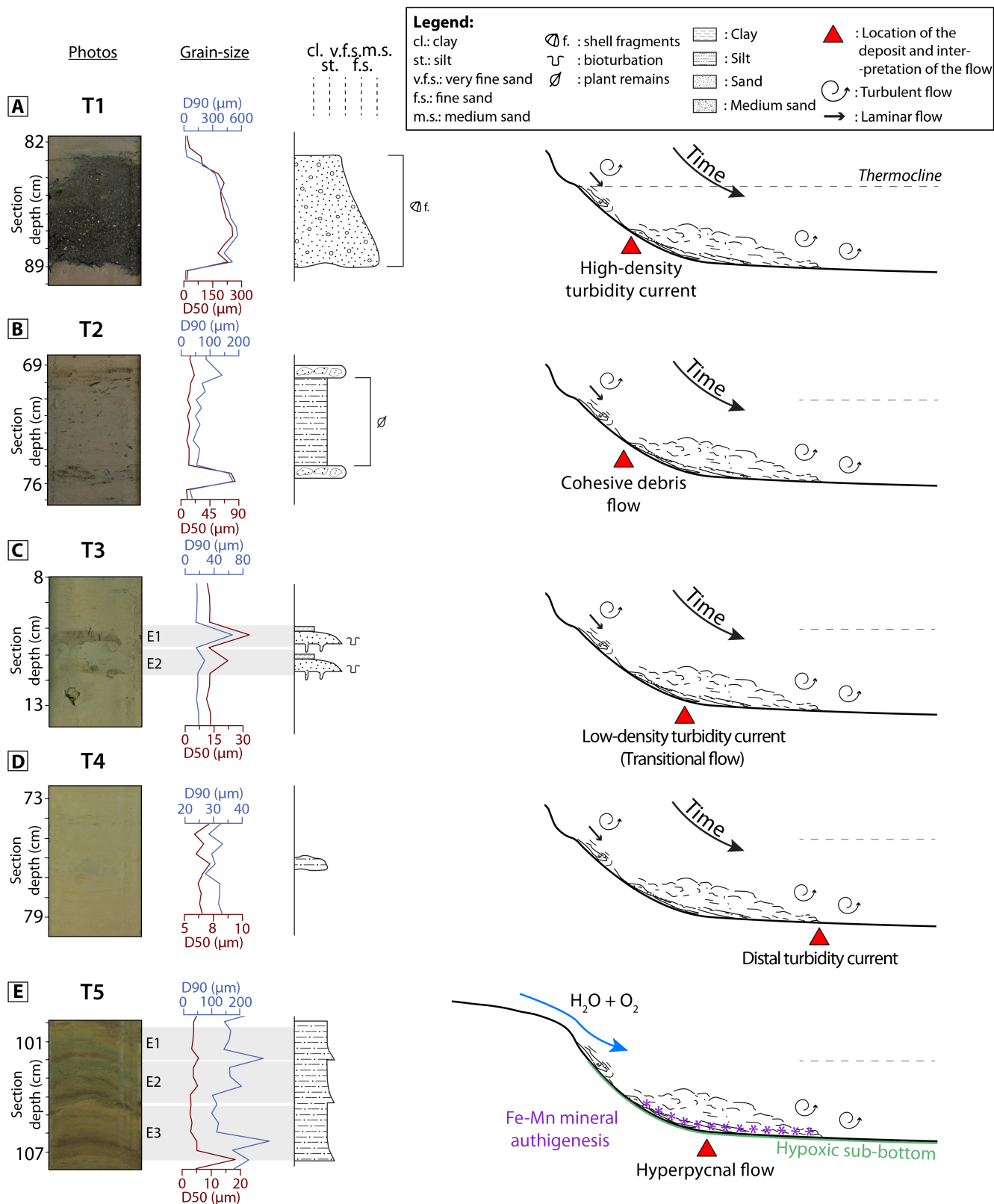
FIGURE 8 Characteristics and interpretation sketches of the five main types of event deposits found in the sediment record of Lake Iznik. From left to right: optical photography, grain-size profiles (D50, D90), drawn according to grain size, and interpretation of the depositional flow process of each event-deposit type. Flow names are given according to Talling et al. (2012).

having cohesive mud contents sufficient to support the sand grain patches observed (Figure 2). There is no unique flow class for a deposit as debris flows are more likely to transform into hyperconcentrated or concentrated density flows, for example, if they contain high proportions of particles larger than medium silt (Hampton, 1972).

However, the lithological structure of one of the three T2 deposits observed in the sediment cores collected in this study (Section 4.2.2) indicates rotational deformation within the layer, such as a reversal sequence (Sabatier et al., 2017; Sauerbrey et al., 2013), which could have originated from the steep south slope or the cliff of the northern underwater terrace (Figures 8B and 6). However, only part of the deposit is reversed here, which can be observed in high-density flows where the upper sandy layer could be a distal deposit of another synchronously triggered flow (Van Daele et al., 2017). Furthermore, the presence of clay is also known to dampen fluid turbulence (Hampton, 1972), resulting in the observed *en masse* deposition. Deposition can occur rapidly in such cases, and sand pulses of synchronously triggered turbidity currents across the basin can be separated by a large amount of homogenous mud (Van Daele et al., 2017). Therefore, these deposits are likely related to cohesive debris/high-density flows where the clay content would have damped the turbulence and generated this *en masse* deposition.

5.2.3 | T3 and T4 depositional processes

The T3 and T4 deposits are overall thinner than the T1 and T2 types (a few millimetres compared to the centimetre scale) (Figures 2 and 8); however, the grain-size patterns (D90/D50 and sorting diagram; Figure 3A,B) show similar characteristics. They have a lower D90 for the same D50 than the T2 deposits, which supports the assumption that T3/4 were deposited by a less cohesive flow (Figure 3B). The thin silty to sandy graded layers of T3, with erosive bases interrupting the background sedimentation, are similar to the deposits from Lake Hazar (type 2; Hage et al., 2017) interpreted as resulting from 'transitional flow characterised by a balance between cohesion and turbulence', corresponding to a surge-like turbidity current (Mulder & Alexander, 2001)/low-density turbidity current (Talling et al., 2012).

On the other hand, T4 deposits are more challenging to identify because they are made of silty lenses and do not contain a basal silty/sandy layer, such as in T3 deposits (Figures 2D and 8C,D). Additionally, T4 deposits are ungraded clayey silt layers that may be similar to another turbidite type documented in Lake Hazar (type 1; Hage et al., 2017), attributed to low-strength cohesive debrites (Talling et al., 2012) which were likely deposited by the

action of turbulent flows that reached more distal locations, associated with the 'terminal cloud' of turbiditic flows, thus corresponding to the distal expression of T3 deposits (Figure 8C,D; Mulder & Alexander, 2001), or even produced by the resuspension of *in situ* unconsolidated fine sediments.

5.2.4 | T5 depositional processes

The T1, T2, T3 and T4 event deposits extend all over the southern subbasin and partially to the north (Figure 4C). The T5 deposits, in contrast, occur only in the lacustrine continuation of the Kara River delta mouth (core IZN19_20), strongly supporting the interpretation that they are deposited by flood-induced hyperpycnal currents that have relatively short run-out distances from river mouths (Mulder & Alexander, 2001). In addition, T5 deposits are better sorted. Based on the D90/D50 diagram, T5 deposits seem to be deposited from a more dilute/turbulent flow than T2 deposits, for example (Figure 3A), which fits previous observations of flood-induced deposits (Beck, 2009). Moreover, T5 deposits generally have more terrigenous content than the other types, suggesting a hyperpycnite origin (Figure 3D,E).

Significant Mn peaks from T5 deposits are observed and related to micro-scale Mn-Fe accumulations occurring on carbonate surfaces, indicating post-depositional changes of the carbonate fraction in these deposits (Figure 2E). Similar signatures have been described in previous studies where peaks in Mn are systematically attributed to flood-induced deposits that have been related to sediment/water transport processes by hyperpycnal currents (Rapuc et al., 2020; Sabatier et al., 2017; Wilhelm et al., 2016a). In some cases, earthquake-generated deposits also present those peaks (Çağatay et al., 2012; Drab et al., 2015; McHugh et al., 2014; Rapuc et al., 2020), as might be the case for the T1 and T4 deposits (Figures 2 and 3). Indeed, they also present a Mn signal, although less prominent than T5 and not systematically observed. If a slope destabilisation is triggered at a depth above the thermocline when the lake is stratified, underwater destabilisation at shallower depths could also bring oxygen to the lake bottom and induce a change in the redox conditions, as observed in Lake du Bourget (Rapuc et al., 2020), which may be the case here and needs to be studied further.

Manganese and Fe patterns in Last Glacial sediments from Lake Iznik (*ca* 18.5 to 27.5 cal years BP) have been previously linked to the authigenic precipitation of rhodochrosite (Mn carbonates), in that case alongside changes in the lakes' seasonal stratification patterns (Roeser et al., 2016). Manganese and Fe are redox-sensitive elements that form

stable Mn(IV) and Fe(III) oxides in oxic waters (Calvert & Pedersen, 1993; Elbaz-Poulichet et al., 2014). Under reducing conditions, Mn and Fe are soluble in the form of Mn(II) and Fe(II) (Davison, 1993; Torres et al., 2014), becoming available for incorporation into authigenic carbonates, for example, formed at redox transitions (Scholtysik et al., 2020). It is suggested that the input of the hyperpycnal sediment plumes from the catchment transported an excess of Mn and Fe oxyhydroxides and some detrital carbonates, which were rapidly deposited in the lake in an event layer (Davison, 1993; Deflandre et al., 2002, Torres et al., 2014; Figure 2). Afterwards, during early diagenesis, under reducing conditions, the dissolution of oxyhydroxides mobilised Mn and Fe ions that eventually adsorbed on the carbonate surfaces. Thus, sedimentological and geochemical evidence indicate that T5 deposits were more likely deposited by hyperpycnal flows during flood events (hyperpycnite; Figure 8E; Mulder & Alexander, 2001).

In addition to the fact that T5 deposits are only observed at the mouth of the Kara River delta, they are observed for a limited interval (13 events between 536 ± 115 cal. CE and 480.5 ± 64.5 cal. CE, i.e. within ca 55 years; Figure 4C). The timing of these flood-induced deposits coincides with a higher background sedimentation rate from ca 350 to ca 600 cal. CE (ca 3 mm/year; Gastineau et al., 2021) during the Late Antiquity. This high sedimentation rate reflects an increase in the erosion rate (Bajard et al., 2016) caused by intense human activities, such as agriculture, as shown by the regional cultivation of olive trees (seen in pollen) during this period (Miebach et al., 2016). Furthermore, several studies have shown that anthropogenic land use induces vegetation-cover modifications, leading to changes in the relationship between precipitation and soil erosion through increased surface run-off. As a result, the flood-frequency signal increases during such a period without any climate modification (Bajard et al., 2020; Brisset et al., 2017; Giguet-Covex et al., 2012), even in large lakes (Rapuc et al., 2019). Nevertheless, it is still surprising to have only deposits for 55 years. It is also possible that the core is sampled at the mouth of a transitional channel in the delta, although this cannot be verified with the current data.

5.3 | Triggers of event deposits

Based on the sediment provenance, the extent of deposition in the lake, and the flow dynamics, T1, T2, T3 and T4 deposits are more likely to result from intrabasinal sediment remobilisations, whereas T5 deposits are more likely flood-induced (Table 2). The single T1 deposit is the coarsest in the dataset (grain size around 200 μm, Figure 3A) and is, therefore, probably related to a particular event, such as a delta collapse, which may be seismic

TABLE 2 Summary table of the characteristics of the five event-deposition types.

Event-deposit type	Location	Number of occurrences	Observed in X/14 cores	Mean thickness (mm)	Synchronous between at least two cores	Related to historical earthquakes	Upward Fining	Mn-Fe carbonates	CLR(Ti$_{mean}$)	CLR(Mn$_{max}$)	ln(Ca/Sr)$_{mean}$
T1	SESB	1	1	60	–	+	+	–	−0.65	−1.01	2.30
T2	NESB SESB	3	3	50	+	+	–	–	−0.53	−0.83	2.14
T3	NESB SESB	~44	9	~5	+	+	+	+	−0.19	−1.24	2.22
T4	NESB SESB	~37	8	~5	+	+	-	+	−0.21	−1.03	2.14
T5	**Delta mouth**	**13**	**1**	**40**	**—**	**—**	**+**	**++**	**0.00**	**−0.72**	**2.69**

Note: The main features that allow deposits to be differentiated are shown. The absence or relative importance of one characteristic for each deposit is denoted as '—', '+' and '++'. In addition, the average values of Ti$_{mean}$, Mn$_{max}$ and ln(Ca/Sr)$_{mean}$ are given. The decisive characteristics that helped distinguish the different triggering mechanisms of event deposits of type T5 from the other types are shown in bold. NESB and SESB refer to the north-eastern and south-eastern subbasins, respectively.

or spontaneous in origin (Girardclos et al., 2007; Hilbe & Anselmetti, 2014). Additional loading after large river discharges can also cause small delta-lip collapses (Clare et al., 2016; Vandekerkhove et al., 2020). The radiocarbon age on top of this only T1 event deposit indicates an age range of 262–537 cal. CE which coincides with a sequence of historical earthquakes that damaged the city of Iznik (e.g. 358 CE, 362 CE, 368 CE, 478 CE; Ambraseys, 2002). An earthquake origin for this deposit is thus likely. The frequent shaking during this period would be sufficient to trigger delta instabilities, making a spontaneous collapse due to overloading more unlikely. Among these earthquakes, the 368 CE one ruptured on the MNAF, while others were recorded on the NNAF. Considering its estimated magnitude (Ms = 6.8) and rupture length (*ca* 30 km) (Wells & Coppersmith, 1994), it could have ruptured the MNAF up to 70 km from the lake, which is still more than the epicentral distance of the other earthquakes that ruptured on the NNAF (358 and 362 CE: 55 km; 478 CE: 35 km). However, the fact that the 368 CE earthquake ruptured the MNAF may favour its record in the lake due to an enhanced peak ground acceleration (Moernaut et al., 2014). Other studies considering rupture direction, wave propagation or intensities that were reached at the lake can help to discriminate which earthquake has been recorded here.

The T2 deposits are observed in three sediment cores and are stratigraphically correlated with the historical earthquake of 1065 CE (Figure 4; Gastineau et al., 2021). The fact that such strong shaking from the Iznik Fault within the lake basin causes specific event deposits might point towards local differences in ground-motion effects. Few studies have indicated that low frequencies remobilise finer, unconsolidated sediments and produce, for example, homogenites. In contrast, high frequencies can produce large-scale erosive and massive turbidites but are quickly attenuated (McHugh et al., 2020; Molenaar et al., 2021). Since the 1065 CE earthquake ruptured the fault in the lake, it is associated with strong ground motion and a wider frequency range (high and low frequencies). Thus, T2 deposits are more likely linked to a slide on a slope or a delta collapse caused by the high-frequency content of this local earthquake.

The stratigraphic correlation highlights the synchronicity of the T3 and T4 deposits associated with the 1065 earthquake. Gastineau et al. (2021) showed that more than 75% of the event deposits in cores IZN19_21 and 31, corresponding to T3 and T4 deposits, fit with historical earthquakes. Most of the 25% remaining event deposits could be related to missing historical chronicles for the older period. Therefore, it is possible to infer that earthquakes have likely generated the older T3 and T4 deposits described in this study. In addition, the high concentrations

of T3 and T4 deposits during the Late Antiquity (3rd–8th century CE) correspond to a higher sedimentation rate of *ca* 3 mm/year (Gastineau et al., 2021) related to a higher erosion rate, similar to the T5 deposits. Therefore, a higher sedimentation rate could have caused slopes to be more sensitive to seismic shaking or spontaneous slope destabilisations (Rapuc et al., 2018; Tournier et al., 2023; Wilhelm et al., 2016a) so that the higher number of turbidites does not necessarily indicate more frequent strong earthquakes in that period. As the sensitivity of the lake to earthquakes depends on the sedimentation rate, caution is required when establishing turbidite-based palaeoseismic records.

To conclude, T1, T2 and T3 were necessarily caused by significant slope destabilisation because they contain sand from the shore. Furthermore, T1 and T2 are recorded in cores very close to slope destabilisation or slopes >30°, except for core IZN19_24 (Figure 6C), compared to T3 and T4 deposits recorded farther from the steepest slopes. Moreover, an interesting observation for future investigation is that T1 and T2 deposits might have been generated by earthquakes rupturing the MNAF (368 and 1065 CE earthquake), unlike the T3 and T4 deposits which could have been generated by earthquakes rupturing either the MNAF or the NNAF, as also shown by Gastineau et al. (2021). This could be, for example, due to longer duration, low-frequency shaking.

5.4 | Spatial distribution of event deposits

Several factors, such as the lake's bathymetry, associated with the length of each sediment core, can explain whether event deposits are recorded in different parts of the basin. For example, two cores collected in the northern subbasin (IZN19_11 and _23; Figure 4) do not show macroscopic evidence of event deposits. In contrast, core IZN19_24, located 2 km to the north-west, documents one T2 deposit, three T3 deposits and nine T4 deposits even though this core is further away from the slope (600 m versus >1 km) and at a similar depth to the two cores that lack event layers (*ca* 55 m depth; Figure 6). Nevertheless, the time record of these sediment cores is quite different (e.g. a few centuries for IZN19_23 compared to two millennia for IZN19_24; Figure 4). However, the lake bottom morphology or the lack of sufficient sediment supply could also explain the lack of event deposits. For cores IZN19_23 and_11, a slight depression exists between the nearest cliffs and the cores, which could have slowed down the turbidite current (Moernaut et al., 2014; Figure 6A,B,C). In addition, isolated core IZN19_09, collected in the lake's

centre at the topographic ridge, records no event deposits during the last 4000 years.

In the southern part of the lake, the cores are very close to steep slopes (15–30°) formed by the active MNAF oblique fault segment, where the most significant amount of deposition is observed. These observations are consistent with the generally accepted concept that the deepest parts of lakes, acting as depocentres, are also the most sensitive locations to record mass-movement deposition due to gravity (Kremer et al., 2015). The deep southern basin of Lake Iznik is also the area with the highest proportion of T1, T2 and T3 deposits over time (IZN19_27; Figure 4D), whereas T4 deposits are more common in the slope-distal areas (e.g. IZN19_31 and _21; Figure 6G).

Notably, a single event does not necessarily have the same sedimentary expression from core to core. For example, based on geochemical data and radiocarbon dating, the single T1 deposit in core IZN19_27 correlates with a T3 deposit in core IZN19_15 located 1.5 km to the east. Similar transitions occur near the Iznik Fault, where a T3 deposit in core IZN19_29 correlates to a T4 deposit in core IZN19_21, an event layer that disappears entirely away from the delta on the southern slope (Figure 4D). Therefore, in that case, the distance to the slope destabilisation seems to be the main factor influencing the type of deposits.

Lateral variations in the presence and/or type of event deposits were a consequence of the 1065 earthquake. For example, the easternmost core IZN19_16 (Figure 7) shows no event deposits correlating with the 1065 CE historical earthquake. Core IZN19_16 is the farthest (1.3 km) from the steep slopes of the southern shore and is located on the hanging wall of the Iznik Fault. As the fault ruptured during this 1065 CE earthquake, the propagation of the turbidity flow could have been slowed down or even stopped by the *ca* 40 cm vertical coseismic offset (Gastineau et al., 2021; Moernaut et al., 2014). Another explanation for deposition variability in these cores could be the distance between the slope destabilisation and the core locations. Cores IZN19_16 and _29 might be too far from the slope destabilisation to record the turbiditic event (Figure 7D,E). The presence and/or thickness of a single turbidite is also influenced by the exact pathways of the turbidity currents, which are controlled by topographical gradients (Moernaut et al., 2014).

All of these spatial observations suggest (i) that the deposits in different cores may have different source areas, although generated by the same event confirming their earthquake origin and (ii) that the difference in event deposit types is rather related to the transformation of the flow with distance from the source of destabilisation (Figure 3E). Of course, other factors such as the sediment rate and lake-floor topography will influence what is preserved in the sediment record.

6 | CONCLUSIONS

This study provides information on the depositional mechanism of extreme geodynamic and climatic events occurring in Lake Iznik. Sediment-core analyses demonstrated that one out of the five types of event deposits (type T5) was deposited by flood-triggered hyperpycnal flows resulting in a distinct geochemical signature, including micro-scale Mn and Fe accumulation on carbonate phases. In contrast, earthquakes generate four other types of event deposits in Lake Iznik with their lithologies depending on their distance to the slope destabilisation or sediment remobilisation process.

A single earthquake can form at least three distinct types of depositional events, possibly depending on the flow mechanism and distance from its source and sedimentation rates, as highlighted by the 1065 CE earthquake. Moreover, this study shows that the 1065 CE earthquake was the only event that generated T2 deposits. This result suggests that this local earthquake caused more significant ground motion, with possibly a broader frequency content (high and low frequencies) that should be further studied. In addition, other parameters (e.g. tsunami, seiche effect) may have been involved, and further studies are needed to better understand their impact on the event deposits. Furthermore, at first sight, the T1 and T2 deposits were likely caused by earthquakes that ruptured the MNAF, which is not the case for T3 and T4 deposits which record earthquakes that ruptured both the NNAF and MNAF, as they are probably associated with the low-frequency content of the earthquake.

CONFLICT OF INTEREST STATEMENT

The authors declare no conflict of interest.

DATA AVAILABILITY STATEMENT

Supplementary data reported in this study are given in the supporting information, and all core and geophysical data are stored in the Pangaea repository at https://doi.org/10.1594/PANGAEA.935167. All cores are registered in the French National Cyber-Core-Repository by APK Corebook (https://www.cybercarotheque.fr, provided by CNRS-OASU-EDYTEM-EPOC), and the persistent sample identifier IGSN was allocated by the French national allocating agent (https://www.igsn.cnrs.fr). The 5 m interval bathymetry of Lake Iznik can be obtained from the Turkish General Directorate of Hydraulic Works (DSI).

ORCID

R. Gastineau https://orcid.org/0000-0002-6283-2852

REFERENCES

Ambraseys, N.N. (2002) The seismic activity of the Marmara Sea region over the last 2000 years. *Bulletin of the Seismological Society of America*, 92, 1–18.

Ambraseys, N.N. & Finkel, C. (1991) Long-term seismicity of Istanbul and of the Marmara Sea region. *Terra Nova*, 3, 527–539.

Ambraseys, N.N. & Jackson, J.A. (2000) Seismicity of the Sea of Marmara (Turkey) since 1500. *Geophysical Journal International*, 141, F1–F6.

Armijo, R., Pondard, N., Meyer, B., Uçarkus, G., de Lépinay, B.M., Malavieille, J., Dominguez, S., Gustcher, M.-A., Schmidt, S., Beck, C., Çagatay, N., Çakir, Z., Imren, C., Eris, K., Natalin, B., Özalaybey, S., Tolun, L., Lefèvre, I., Seeber, L., Gasperini, L., Rangin, C., Emre, O. & Sarikavak, K. (2005) Submarine fault scarps in the Sea of Marmara pull-apart (North Anatolian Fault): Implications for seismic hazard in Istanbul. *Geochemistry, Geophysics, Geosystems*, 6, Q06009. https://doi.org/10.1029/2004GC000896

Arnaud, F., Révillon, S., Debret, M., Revel, M., Chapron, E., Jacob, J., Giguet-Covex, C., Poulenard, J. & Magny, M. (2012) Lake Bourget regional erosion patterns reconstruction reveals Holocene NW European Alps soil evolution and paleohydrology. *Quaternary Science Reviews*, 51, 81–92.

Avşar, U., Hubert-Ferrari, A., De Batist, M., Schmidt, S. & Fagel, N. (2015) Sedimentary records of past earthquakes in Boraboy Lake during the last ca 600 years (North Anatolian Fault, Turkey). *Palaeogeography, Palaeoclimatology, Palaeoecology*, 433, 1–9.

Bajard, M., Poulenard, J., Sabatier, P., Bertrand, Y., Crouzet, C., Ficetola, G.F., Blanchet, C., Messager, E., Giguet-Covex, C.,

Gielly, L., Rioux, D., Chen, W., Malet, E., Develle, A.-L. & Arnaud, F. (2020) Pastoralism increased vulnerability of a sub-alpine catchment to flood hazard through changing soil properties. *Palaeogeography, Palaeoclimatology, Palaeoecology*, 538, 109462.

Bajard, M., Sabatier, P., David, F., Develle, A.-L., Reyss, J.-L., Fanget, B., Malet, E., Arnaud, D., Augustin, L., Crouzet, C., Poulenard, J. & Arnaud, F. (2016) Erosion record in Lake La Thuile sediments (Prealps, France): evidence of montane landscape dynamics throughout the Holocene. *The Holocene*, 26, 350–364.

Beck, C. (2009) Late Quaternary lacustrine paleo-seismic archives in north-western Alps: examples of earthquake-origin assessment of sedimentary disturbances. *Earth-Science Reviews*, 96, 327–344.

Benjelloun, Y. (2017) The middle strand of the North Anatolian fault in Iznik region: insights from geomorphology and archeoseismology. Doctoral dissertation, Université Grenoble Alpes.

Benjelloun, Y., De Sigoyer, J., Dessales, H., Baillet, L., Guéguen, P. & Şahin, M. (2020) Historical earthquake scenarios for the middle strand of the North Anatolian Fault deduced from archeo-damage inventory and building deformation modeling.

Benjelloun, Y., de Sigoyer, J., Garambois, S., Carcaillet, J. & Klinger, Y. (2021) Segmentation and Holocene behavior of the middle strand of the North Anatolian Fault (NW Turkey). *Tectonics*, 40, e2021TC006870.

Bertrand, S., Hughen, K.A., Sepúlveda, J. & Pantoja, S. (2012) Geochemistry of surface sediments from the fjords of Northern Chilean Patagonia (44–47°S): spatial variability and implications for paleoclimate reconstructions. *Geochimica et Cosmochimica Acta*, 76, 125–146.

Blott, S.J. & Pye, K. (2001) GRADISTAT: a grain size distribution and statistics package for the analysis of unconsolidated sediments. *Earth Surface Processes and Landforms*, 26, 1237–1248.

Bøe, A.-G., Dahl, S.O., Lie, Ø. & Nesje, A. (2006) Holocene river floods in the upper Glomma catchment, southern Norway: a high-resolution multiproxy record from lacustrine sediments. *The Holocene*, 16, 445–455.

Brisset, E., Guiter, F., Miramont, C., Troussier, T., Sabatier, P., Poher, Y., Cartier, R., Arnaud, F., Malet, E. & Anthony, E.J. (2017) The overlooked human influence in historic and prehistoric floods in the European Alps. *Geology*, 45, 347–350.

Çağatay, M., Erel, L., Bellucci, L., Polonia, A., Gasperini, L., Eriş, K., Sancar, Ü., Biltekin, D., Uçarkuş, G., Ülgen, U. & Damcı, E. (2012) Sedimentary earthquake records in the İzmit gulf, sea of Marmara, Turkey. *Sedimentary Geology*, 282, 347–359.

Çağatay, M.N. & Uçarkuş, G. (2019) Morphotectonics of the Sea of Marmara: basins and highs on the North Anatolian continental transform plate boundary. In: Duarte, J.C. (Ed.) *Transform plate boundaries and fracture zones*. Amsterdam: Elsevier, pp. 397–416.

Çağatay, M.N., Wulf, S., Sancar, Ü., Özmaral, A., Vidal, L., Henry, P., Appelt, O. & Gasperini, L. (2015) The tephra record from the Sea of Marmara for the last ca. 70 ka and its palaeoceanographic implications. *Marine Geology*, 361, 96–110.

Calvert, S. & Pedersen, T. (1993) Geochemistry of recent oxic and anoxic marine sediments: implications for the geological record. *Marine Geology*, 113, 67–88.

Chapron, E., Beck, C., Pourchet, M. & Deconinck, J.-F. (1999) 1822 earthquake-triggered homogenite in Lake Le Bourget (NW Alps). *Terra Nova*, 11, 86–92.

Chapron, E., Simonneau, A., Ledoux, G., Arnaud, F., Lajeunesse, P. & Albéric, P. (2016) French Alpine foreland holocene paleoseismicity revealed by coeval mass wasting deposits in glacial lakes. In: Lamarche, G., Mountjoy, J., Bull, S., Hubble, T., Krastel, S., Lane, E., Micallef, A., Moscardelli, L., Mueller, C., Pecher, I. & Woelz, S. (Eds.) *Submarine mass movements and their consequences*. Advances in Natural and Technological Hazards Research, vol 41. Cham: Springer. Available from: https://doi.org/10.1007/978-3-319-20979-1_34

Clare, M.A., Hughes Clarke, J.E., Talling, P.J., Cartigny, M.J.B. & Pratomo, D.G. (2016) Preconditioning and triggering of offshore slope failures and turbidity currents revealed by most detailed monitoring yet at a fjord-head delta. *Earth and Planetary Science Letters*, 450, 208–220.

Davison, W. (1993) Iron and manganese in lakes. *Earth-Science Reviews*, 34, 119–163.

Deflandre, B., Mucci, A., Gagné, J.-P., Guignard, C. & Jørn Sundby, B. (2002) Early diagenetic processes in coastal marine sediments disturbed by a catastrophic sedimentation event. *Geochimica et Cosmochimica Acta*, 66, 2547–2558.

Doğan, B., Tüysüz, O. & Şanlı, F.B. (2015) Tectonostratigraphic evolution of the basins on the southern branch of the North Anatolian Fault System in the SE Marmara Region, Turkey. *International Journal of Earth Sciences*, 104, 389–418.

Drab, L., Hubert, A., Schmidt, S. & Martinez, P. (2012) The earthquake sedimentary record in the western part of the Sea of Marmara, Turkey. *Natural Hazards and Earth System Sciences*, 12(4), 1235–1254. https://doi.org/10.5194/nhess-12-1235-2012

Drab, L., Hubert-Ferrari, A., Schmidt, S., Martinez, P., Carlut, J. & Ouahabi, M.E. (2015) Submarine earthquake history of the Çınarcık segment of the North Anatolian Fault in the Marmara Sea, Turkey. *Bulletin of the Seismological Society of America*, 105, 622–645.

Elbaz-Poulichet, F., Sabatier, P., Dezileau, L. & Freydier, R. (2014) Sedimentary record of V, U, Mo and Mn in the Pierre-Blanche lagoon (Southern France)–Evidence for a major anoxia event during the Roman period. *The Holocene*, 24, 1384–1392.

Folk, R.L. & Ward, W.C. (1957) Brazos River bar [Texas]: a study in the significance of grain size parameters. *Journal of Sedimentary Research*, 27, 3–26.

Franz, S.O., Schwark, L., Brüchmann, C., Scharf, B., Klingel, R., Van Alstine, J.D., Çagatay, N. & Ülgen, U.B. (2006) Results from a multi-disciplinary sedimentary pilot study of Tectonic Lake Iznik (NW Turkey)—geochemistry and paleolimnology of the recent past. *J Paleolimnol*, 35, 715–736.

Gastineau, R., De Sigoyer, J., Sabatier, P., Fabbri, S.C., Anselmetti, F.S., Develle, A.L., Şahin, M., Gündüz, S., Niessen, F. & Gebhardt, A.C. (2021) Active subaquatic fault segments in Lake Iznik along the middle strand of the North Anatolian Fault, NW Turkey. *Tectonics*, 40, e2020TC006404.

Giguet-Covex, C., Arnaud, F., Enters, D., Poulenard, J., Millet, L., Francus, P., David, F., Rey, P.-J., Wilhelm, B. & Delannoy, J.-J. (2012) Frequency and intensity of high-altitude floods over the last 3.5 ka in northwestern French Alps (Lake Anterne). *Quaternary Research*, 77, 12–22.

Girardclos, S., Schmidt, O.T., Sturm, M., Ariztegui, D., Pugin, A. & Anselmetti, F.S. (2007) The 1996 AD delta collapse and large turbidite in Lake Brienz. *Marine Geology*, 241, 137–154.

Hage, S., Hubert-Ferrari, A., Lamair, L., Avşar, U., El Ouahabi, M., Van Daele, M., Boulvain, F., Ali Bahri, M., Seret, A. & Plenevaux, A. (2017) Flow dynamics at the origin of thin clayey sand lacustrine turbidites: examples from Lake Hazar, Turkey. *Sedimentology*, 64, 1929–1956.

Hampton, M.A. (1972) The role of subaqueous debris flow in generating turbidity currents. *Journal of Sedimentary Petrology*, 42, 775–793.

Haughton, P., Davis, C., McCaffrey, W. & Barker, S. (2009) Hybrid sediment gravity flow deposits–classification, origin and significance. *Marine and Petroleum Geology*, 26, 1900–1918.

Heiri, O., Lotter, A.F. & Lemcke, G. (2001) Loss on ignition as a method for estimating organic and carbonate content in sediments: reproducibility and comparability of results. *Journal of Paleolimnology*, 25, 101–110.

Henry, P., Sinan Özeren, M., Yakupoğlu, N., Çakir, Z., de Saint-Léger, E., de Gésincourt, O.D., Tengberg, A., Chevalier, C., Papoutsellis, C., Postacıoğlu, N., Dogan, U., Karabulut, H., Uçarkuş, G. & Çağatay, M.N. (2022) Mass flows, turbidity currents and other hydrodynamic consequences of small and moderate earthquakes in the Sea of Marmara. *Natural Hazards and Earth System Sciences*, 22(12), 3939–3956.

Hilbe, M. & Anselmetti, F.S. (2014) Signatures of slope failures and river-delta collapses in a perialpine lake (Lake Lucerne, Switzerland). *Sedimentology*, 61, 1883–1907.

Jenny, J.-P., Wilhelm, B., Arnaud, F., Sabatier, P., Giguet Covex, C., Mélo, A., Fanget, B., Malet, E., Ployon, E. & Perga, M.E. (2014) A 4D sedimentological approach to reconstructing the flood frequency and intensity of the Rhône River (Lake Bourget, NW European Alps). *Journal of Paleolimnology*, 51, 469–483.

Jochum, K.P., Dingwell, D.B., Rocholl, A., Stoll, B., Hofmann, A.W., Becker, S., Besmehn, A., Bessette, D., Dietze, H.-J., Dulski, P., Erzinger, J., Hellebrand, E., Hoppe, P., Horn, I., Janssens, K., Jenner, G.A., Klein, M., McDonough, W.F., Maetz, M., Mezger, K., Müker, C., Nikogosian, I.K., Pickhardt, C., Raczek, I., Rhede, D., Seufert, H.M., Simakin, S.G., Sobolev, A.V., Spettel, B., Straub, S. & Vincz, L. (2000) The preparation and preliminary characterisation of eight geological MPI-DING reference glasses for in-situ microanalysis. *Geostandards Newsletter*, 24, 87–133.

Jochum, K.P., Nohl, U., Herwig, K., Lammel, E., Stoll, B. & Hofmann, A.W. (2005) GeoReM: a new geochemical database for reference materials and isotopic standards. *Geostandards and Geoanalytical Research*, 29, 333–338.

Kremer, K., Corella, J.P., Adatte, T., Garnier, E., Zenhäusern, G. & Girardclos, S. (2015) Origin of turbidites in deep Lake Geneva (France–Switzerland) in the last 1500 years. *Journal of Sedimentary Research*, 85, 1455–1465.

Kremer, K., Wirth, S.B., Reusch, A., Fäh, D., Bellwald, B., Anselmetti, F.S., Girardclos, S. & Strasser, M. (2017) Lake-sediment based paleoseismology: limitations and perspectives from the Swiss Alps. *Quaternary Science Reviews*, 168, 1–18.

Le Maitre, R., Bateman, P., Dudek, A., Keller, J., Lameyre Le Bas, M.J., Sabine, P.A., Schmid, R., Sorensen, H., Streckeisen, A., Woolley, A.R., Lameyre Le Bas MJ, Z.B., Sabine, P.A., Schmid, R., Sorensen, H., Streckeisen, A., Woolley, A.R. & Zanettin, B. (1989) *A classification of igneous rocks and glossary of terms*. Oxford: *Blackwell*.

Lê, S., Josse, J. & Husson, F. (2008) FactoMineR: An R package for multivariate analysis. *Journal of Statistical Software*, 25(1), 1–18. https://doi.org/10.18637/jss.v025.i01

Lu, Y., Waldmann, N., Ian Alsop, G. & Marco, S. (2017) Interpreting soft sediment deformation and mass transport deposits as

seismites in the dead sea depocenter. *Journal of Geophysical Research: Solid Earth*, 122, 8305–8325.

McHugh, C.M., Kanamatsu, T., Seeber, L., Bopp, R., Cormier, M.-H. & Usami, K. (2016) Remobilization of surficial slope sediment triggered by the AD 2011 Mw 9 Tohoku-Oki earthquake and tsunami along the Japan Trench. *Geology*, 44, 391–394.

McHugh, C.M., Seeber, L., Cormier, M.-H., Dutton, J., Cagatay, N., Polonia, A., Ryan, W.B. & Gorur, N. (2006) Submarine earthquake geology along the North Anatolia Fault in the Marmara Sea, Turkey: a model for transform basin sedimentation. *Earth and Planetary Science Letters*, 248, 661–684.

McHugh, C.M., Seeber, L., Cormier, M.-H. & Hornbach, M. (2014) Submarine paleoseismology along populated transform boundaries: the Enriquillo-plantain-garden fault, Canal du Sud, Haiti, and the north Anatolian fault, Marmara Sea, Turkey. *Oceanography*, 27, 118–131.

McHugh, C.M., Seeber, L., Rasbury, T., Strasser, M., Kioka, A., Kanamatsu, T., Ikehara, K. & Usami, K. (2020) Isotopic and sedimentary signature of megathrust ruptures along the Japan subduction margin. *Marine Geology*, 428, 106283.

Metrich, N. & Rutherford, M. (1992) Experimental study of chlorine behavior in hydrous silicic melts. *Geochimica et Cosmochimica Acta*, 56, 607–616.

Miebach, A., Niestrath, P., Roeser, P. & Litt, T. (2016) Impacts of climate and humans on the vegetation in northwestern Turkey: palynological insights from Lake Iznik since the Last Glacial. *Climate of the Past*, 12, 575–593.

Moernaut, J., Daele, M.V., Heirman, K., Fontijn, K., Strasser, M., Pino, M., Urrutia, R. & Batist, M.D. (2014) Lacustrine turbidites as a tool for quantitative earthquake reconstruction: new evidence for a variable rupture mode in south central Chile. *Journal of Geophysical Research: Solid Earth*, 119, 1607–1633.

Moernaut, J., Van Daele, M., Strasser, M., Clare, M.A., Heirman, K., Viel, M., Cardenas, J., Kilian, R., Ladrón de Guevara, B., Pino, M., Urrutia, R. & De Batist, M. (2017) Lacustrine turbidites produced by surficial slope sediment remobilization: a mechanism for continuous and sensitive turbidite paleoseismic records. *Marine Geology*, 384, 159–176.

Molenaar, A., Van Daele, M., Vandorpe, T., Degenhart, G., De Batist, M., Urrutia, R., Pino, M., Strasser, M. & Moernaut, J. (2021) What controls the remobilization and deformation of surficial sediment by seismic shaking? Linking lacustrine slope stratigraphy to great earthquakes in South–Central Chile. *Sedimentology*, 68, 2365–2396. https://doi.org/10.1111/sed.12856

Molinaroli, E., Guerzoni, S., De Falco, G., Sarretta, A., Cucco, A., Como, S., Simeone, S., Perilli, A. & Magni, P. (2009) Relationships between hydrodynamic parameters and grain size in two contrasting transitional environments: the Lagoons of Venice and Cabras, Italy. *Sedimentary Geology*, 219, 196–207.

Mulder, T. & Alexander, J. (2001) The physical character of subaqueous sedimentary density flows and their deposits. *Sedimentology*, 48, 269–299.

Munsell Color. (1994) *Munsell soil color charts*. Baltimore, MD: Munsell Color.

Öztürk, K., Yaltirak, C. & Alpar, B. (2009) The Relationship Between the Tectonic Setting of the Lake İznik Basin and the Middle Strand of the North Anatolian Fault. *Turkish Journal of Earth Sciences*, 18(2), Article 3. https://doi.org/10.3906/yer-0803-4, https://journals.tubitak.gov.tr/earth/vol18/iss2/3

Parris, A.S., Bierman, P.R., Noren, A.J., Prins, M.A. & Lini, A. (2010) Holocene paleostorms identified by particle size signatures in lake sediments from the northeastern United States. *Journal of Paleolimnology*, 43, 29–49.

Passega, R. (1964) Grain size representation by CM pattern as a geologic tool. *Journal of Sedimentry Petrology*, 34, 830–847.

Polonia, A., Nelson, C.H., Romano, S., Vaiani, S.C., Colizza, E., Gasparotto, G. & Gasperini, L. (2017) A depositional model for seismo-turbidites in confined basins based on Ionian Sea deposits. *Marine Geology*, 384, 177–198.

Praet, N., Moernaut, J., Van Daele, M., Boes, E., Haeussler, P.J., Strupler, M., Schmidt, S., Loso, M.G. & De Batist, M. (2017) Paleoseismic potential of sublacustrine landslide records in a high-seismicity setting (south-central Alaska). *Marine Geology*, 384, 103–119.

Praet, N., Van Daele, M., Collart, T., Moernaut, J., Vandekerkhove, E., Kempf, P., Haeussler, P.J. & De Batist, M. (2020) Turbidite stratigraphy in proglacial lakes: deciphering trigger mechanisms using a statistical approach. *Sedimentology*, 67, 2332–2359.

R Core Team. (2018) *R: a language and environment for statistical computing*. Vienna, Austria: R Foundation for Statistical Computing.

Rapuc, W., Arnaud, F., Sabatier, P., Anselmetti, F.S., Piccin, A., Peruzza, L., Bastien, A., Augustin, L., Régnier, E., Gaillardet, J. & Von Grafenstein, U. (2022) Instant sedimentation in a deep Alpine lake (Iseo, Italy) controlled by climate, human and geodynamic forcing. *Sedimentology*, 69, 1816–1840. https://doi.org/10.1111/sed.12972

Rapuc, W., Jacq, K., Develle-Vincent, A.-L., Sabatier, P., Fanget, B., Perrette, Y., Coquin, D., Debret, M., Wilhelm, B. & Arnaud, F. (2020) XRF and hyperspectral analyses as an automatic way to detect flood events in sediment cores. *Sedimentary Geology*, 409, 105776.

Rapuc, W., Sabatier, P., Andrič, M., Crouzet, C., Arnaud, F., Chapron, E., Šmuc, A., Develle, A.-L., Wilhelm, B., Demory, F., Reyss, J.-L., Régnier, E., Daut, G. & Von Grafenstein, U. (2018) 6600 years of earthquake record in the Julian Alps (Lake Bohinj, Slovenia). *Sedimentology*, 65, 1777–1799.

Rapuc, W., Sabatier, P., Arnaud, F., Palumbo, A., Develle, A.-L., Reyss, J.-L., Augustin, L., Régnier, E., Piccin, A., Chapron, E., Dumoulin, J.-P. & von Grafenstein, U. (2019) Holocene-long record of flood frequency in the Southern Alps (Lake Iseo, Italy) under human and climate forcing. *Global and Planetary Change*, 175, 160–172.

Reilinger, R., McClusky, S., Vernant, P., Lawrence, S., Ergintav, S., Cakmak, R., Ozener, H., Kadirov, F., Guliev, I., Stepanyan, R., Nadariya, M., Hahubia, G., Salah, M., Sakr, K., ArRajehi, A., Demitris, P., Al-Aydrus, A., Prilepin, M., Guseva, T., Evren, E., Andriy, D., Filikov, S.V., Gomez, F., Al-Ghazzi, R. & Karam, G. (2006) GPS constraints on continental deformation in the Africa-Arabia-Eurasia continental collision zone and implications for the dynamics of plate interactions. *Journal of Geophysical Research*, 111, B05411. https://doi.org/10.1029/2005JB004051

Reimer, P., Austin, W., Bard, E., Bayliss, A., Blackwell, P., Bronk Ramsey, C., Butzin, M., Cheng, H., Lawrence Edwards, R., Friedrich, M., Grootes, P.M., Guilderson, T.P., Hajdas, I., Heaton, T.J., Hogg, A.G., Hughen, K.A., Kromer, B., Manning, S.W., Muscheler, R., Palmer, J.G., Pearson, C., van der Plicht, J., Reimer, R.W., Richards, D.A., Scott, E.M., Southon, J.R., Turney, C.S.M., Wacker, L., Adolphi, F., Büntgen, U., Capano, M., Fahrni,

S.M., Fogtmann-Schulz, A., Friedrich, R., Köhler, P., Kudsk, S., Miyake, F., Olsen, J., Reinig, F., Sakamoto, M. & SookdeoTalamo, A. (2020) The IntCal20 Northern Hemisphere Radiocarbon Age Calibration Curve (0–55 cal kBP). *Radiocarbon*, 62(4), 725–757. https://doi.org/10.1017/RDC.2020.41

Richter, T.O., Van der Gaast, S., Koster, B., Vaars, A., Gieles, R., de Stigter, H.C., De Haas, H. & van Weering, T.C. (2006) The Avaatech XRF Core Scanner: technical description and applications to NE Atlantic sediments. *Geological Society, London, Special Publications*, 267, 39–50.

Roeser, P. (2014) Paleolimnology of Lake Iznik (NW Turkey) during the past 31 ka cal BP. Doctoral dissertation, Bonn.

Roeser, P., Franz, S.O. & Litt, T. (2016) Aragonite and calcite preservation in sediments from Lake Iznik related to bottom lake oxygenation and water column depth. *Sedimentology*, 63, 2253–2277.

Roeser, P., Franz, S.O., Litt, T., Ülgen, U.B., Hilgers, A., Wulf, S., Wennrich, V., Akçer Ön, S., Viehberg, F.A., Çağatay, M.N. & Melles, M. (2012) Lithostratigraphic and geochronological framework for the paleoenvironmental reconstruction of the last ~36 ka cal BP from a sediment record from Lake Iznik (NW Turkey). *Quaternary International*, 274, 73–87.

Sabatier, P., Dezileau, L., Briqueu, L., Colin, C. & Siani, G. (2010) Clay minerals and geochemistry record from northwest Mediterranean coastal lagoon sequence: implications for paleostorm reconstruction. *Sedimentary Geology*, 228, 205–217.

Sabatier, P., Moernaut, J., Bertrand, S., Van Daele, M., Kremer, K., Chaumillon, E. & Arnaud, F. (2022) A review of event deposits in lake sediments. *Quaternary*, 5, 34.

Sabatier, P., Wilhelm, B., Ficetola, G.F., Moiroux, F., Poulenard, J., Develle, A.-L., Bichet, A., Chen, W., Pignol, C., Reyss, J.-L., Gielly, L., Bajard, M., Perrette, Y., Malet, E., Taberlet, P. & Arnaud, F. (2017) 6-kyr record of flood frequency and intensity in the western Mediterranean Alps—Interplay of solar and temperature forcing. *Quaternary Science Reviews*, 170, 121–135.

Sarı, E. & Çağatay, M.N. (2006) Turbidites and their association with past earthquakes in the deep Çınarcık Basin of the Marmara Sea. *Geo-Marine Letters*, 26, 69–76.

Sauerbrey, M., Juschus, O., Gebhardt, A., Wennrich, V., Nowaczyk, N. & Melles, M. (2013) Mass movement deposits in the 3.6 Ma sediment record of Lake El'gygytgyn, far east Russian Arctic. *Climate of the Past*, 9, 1949–1967.

Scholtysik, G., Dellwig, O., Roeser, P., Arz, H.W., Casper, P., Herzog, C., Goldhammer, T. & Hupfer, M. (2020) Geochemical focusing and sequestration of manganese during eutrophication of Lake Stechlin (NE Germany). *Biogeochemistry*, 151, 313–334.

Şengör, A.C. & Yilmaz, Y. (1981) Tethyan evolution of Turkey: a plate tectonic approach. *Tectonophysics*, 75, 181–241.

Sevink, J., van Bergen, M.J., van der Plicht, J., Feiken, H., Anastasia, C. & Huizinga, A. (2011) Robust date for the bronze age Avellino eruption (Somma-Vesuvius): 3945 ±10 calBP (1995 ±10 calBC). *Quaternary Science Reviews*, 30, 1035–1046.

Stein, R.S., Barka, A.A. & Dieterich, J.H. (1997) Progressive failure on the North Anatolian fault since 1939 by earthquake stress triggering. *Geophysical Journal International*, 128, 594–604.

Strasser, M., Monecke, K., Schnellmann, M. & Anselmetti, F.S. (2013) Lake sediments as natural seismographs: a compiled record of Late Quaternary earthquakes in Central Switzerland and its implication for Alpine deformation. *Sedimentology*, 60, 319–341.

Sturm, M. & Matter, A. (1978) Turbidites and varves in Lake Brienz (Switzerland): deposition of clastic detritus by density currents. In: Matter, A. & Tucker, M.E. (Eds.) *Modern and ancient lake sediments*, 1st edition. London: Blackwell Scientific Publications, pp. 147–168.

Talling, P.J., Masson, D.G., Sumner, E.J. & Malgesini, G. (2012) Subaqueous sediment density flows: depositional processes and deposit types. *Sedimentology*, 59, 1937–2003.

Torres, N.T., Och, L.M., Hauser, P.C., Furrer, G., Brandl, H., Vologina, E., Sturm, M., Bürgmann, H. & Müller, B. (2014) Early diagenetic processes generate iron and manganese oxide layers in the sediments of Lake Baikal, Siberia. *Environmental Science: processes & impacts*, 16, 879–889.

Tournier, N., Fabbri, S.C., Anselmetti, F.S., Cahyarini, S.Y., Bijaksana, S., Wattrus, N., Russell, J.M. & Vogel, H. (2023) Climate-controlled sensitivity of lake sediments to record earthquake-related mass wasting in tropical Lake Towuti during the past 40 kyr. *Quaternary Science Reviews*, 305, 108015.

Ülgen, U.B., Franz, S.O., Biltekin, D., Çağatay, M.N., Roeser, P.A., Doner, L. & Thein, J. (2012) Climatic and environmental evolution of Lake Iznik (NW Turkey) over the last ~4700 years. *Quaternary International*, 274, 88–101.

Van Daele, M., Araya-Cornejo, C., Pille, T., Vanneste, K., Moernaut, J., Schmidt, S., Kempf, P., Meyer, I. & Cisternas, M. (2019) Distinguishing intraplate from megathrust earthquakes using lacustrine turbidites. *Geology*, 47, 127–130.

Van Daele, M., Meyer, I., Moernaut, J., De Decker, S., Verschuren, D. & De Batist, M. (2017) A revised classification and terminology for stacked and amalgamated turbidites in environments dominated by (hemi) pelagic sedimentation. *Sedimentary Geology*, 357, 72–82.

Vandekerkhove, E., Van Daele, M., Praet, N., Cnudde, V., Haeussler, P.J. & De Batist, M. (2020) Flood-triggered versus earthquake-triggered turbidites: a sedimentological study in clastic lake sediments (Eklutna Lake, Alaska). *Sedimentology*, 67, 364–389.

Vanneste, K., Wils, K. & Van Daele, M. (2018) Probabilistic evaluation of fault sources based on paleoseismic evidence from mass-transport deposits: the example of Aysén Fjord, Chile. *Journal of Geophysical Research: Solid Earth*, 123, 9842–9865.

Viehberg, F.A., Ülgen, U.B., Damcı, E., Franz, S.O., Ön, S.A., Roeser, P.A., Çağatay, M.N., Litt, T. & Melles, M. (2012) Seasonal hydrochemical changes and spatial sedimentological variations in Lake Iznik (NW Turkey). *Quaternary International*, 274, 102–111.

Wells, D.L. & Coppersmith, K.J. (1994) New empirical relationships among magnitude, rupture length, rupture width, rupture area, and surface displacement. *Bulletin of the Seismological Society of America*, 84, 974–1002.

Weltje, G., Bloemsma, M., Tjallingii, R., Heslop, D., Röhl, U. & Croudace, I. (2015) Prediction of geochemical composition from XRF core scanner data: a new multivariate approach including automatic selection of calibration samples and quantification of uncertainties. In: Croudace, I. & Rothwell, R. (Eds.) *Micro-XRF studies of sediment cores*. Developments in Paleoenvironmental Research, vol. 17. Dordrecht: Springer. https://doi.org/10.1007/978-94-017-9849-5_21

Weltje, G.J. & Tjallingii, R. (2008) Calibration of XRF core scanners for quantitative geochemical logging of sediment cores:

theory and application. *Earth and Planetary Science Letters*, 274, 423–438.

Wilhelm, B., Arnaud, F., Sabatier, P., Magand, O., Chapron, E., Courp, T., Tachikawa, K., Fanget, B., Malet, E., Pignol, C., Bard, E. & Delannoy, J.J. (2013) Palaeoflood activity and climate change over the last 1400 years recorded by lake sediments in the north-west European Alps. *Journal of Quaternary Science*, 28, 189–199.

Wilhelm, B., Nomade, J., Crouzet, C., Litty, C., Sabatier, P., Belle, S., Rolland, Y., Revel, M., Courboulex, F., Arnaud, F. & Anselmetti, F.S. (2016) Quantified sensitivity of small lake sediments to record historic earthquakes: implications for paleoseismology: lake sensitivity to record earthquakes. *Journal of Geophysical Research: Earth Surface*, 121, 2–16.

Wilhelm, B., Sabatier, P. & Arnaud, F. (2015) Is a regional flood signal reproducible from lake sediments? *Sedimentology*, 62, 1103–1117.

Wilhelm, B., Vogel, H., Crouzet, C., Etienne, D. & Anselmetti, F. (2016) Frequency and intensity of palaeofloods at the interface of Atlantic and Mediterranean climate domains. *Climate of the Past*, 12, 299–316.

Yakupoğlu, N., Henry, P., Uçarkuş, G., Eriş, K.K., Demory, F., Crouzet, C. & Çağatay, M.N. (2022) Factors affecting thickness and frequency of turbidites triggered by earthquakes in Kumburgaz Basin, Sea of Marmara. *Marine Geology*, 452, 106900.

Yakupoğlu, N., Uçarkuş, G., Eriş, K.K., Henry, P. & Çağatay, M.N. (2019) Sedimentological and geochemical evidence for seismoturbidite generation in the Kumburgaz Basin, Sea of Marmara: implications for earthquake recurrence along the Central High Segment of the North Anatolian Fault. *Sedimentary Geology*, 380, 31–44.

Zitter, T.A.C., Grall, C., Henry, P., Özeren, M.S., Çağatay, M.N., Şengör, A.M.C., Gasperini, L., de Lépinay, B.M. & Géli, L. (2012) Distribution, morphology and triggers of submarine mass wasting in the Sea of Marmara. *Marine Geology*, 329–331, 58–74.

SUPPORTING INFORMATION

Additional supporting information can be found online in the Supporting Information section at the end of this article.